IMMUNOLOGY

Spatially resolved immune exhaustion within the alloreactive microenvironment predicts liver transplant rejection

Arianna Barbetta[1]†, Brittany Rocque[1]†, Sarah Bangerth[1], Kelly Street[2], Carly Weaver[3], Shefali Chopra[4], Janet Kim[1], Linda Sher[1], Brice Gaudilliere[5], Omid Akbari[6,7], Rohit Kohli[3,8], Juliet Emamaullee[1,6,8]*

Allograft rejection is common following clinical organ transplantation, but defining specific immune subsets mediating alloimmunity has been elusive. Calcineurin inhibitor dose escalation, corticosteroids, and/or lymphocyte depleting antibodies have remained the primary options for treatment of clinical rejection episodes. Here, we developed a highly multiplexed imaging mass cytometry panel to study the immune response in archival biopsies from 79 liver transplant (LT) recipients with either no rejection (NR), acute T cell–mediated rejection (TCMR), or chronic rejection (CR). This approach generated a spatially resolved proteomic atlas of 461,816 cells (42 phenotypes) derived from 96 pathologist-selected regions of interest. Our analysis revealed that regulatory (HLADR$^+$ T$_{reg}$) and PD1$^+$ T cell phenotypes (CD4$^+$ and CD8$^+$ subsets), combined with variations in M2 macrophage polarization, were a unique signature of active TCMR. These data provide insights into the alloimmune microenvironment in clinical LT, including identification of potential targets for focused immunotherapy during rejection episodes and suggestion of a substantial role for immune exhaustion in TCMR.

INTRODUCTION

T cell–mediated rejection (TCMR) remains the most frequent complication after liver transplantation (LT), occurring within the first 6 months in up to 35% of adult LT recipients (*1*–*3*). While TCMR is generally responsive to treatment with pulse corticosteroids, adjustment of maintenance immunosuppression regimens is key for preventing future TCMR episodes (*4*). Ultimately, up to 10% of patients will develop steroid resistance and have recurrent episodes of TCMR. The diagnosis of TCMR hinges upon histological examination of a core biopsy stained with hematoxylin and eosin by a clinical pathologist using rejection activity index (RAI), a composite score ranging from 0 to 9 based on severity of portal inflammation, bile duct inflammation, and venous endotheliitis (*5*, *6*). After its inception following a Banff consensus conference in 1995, the RAI has become the gold standard to establish the diagnosis of TCMR and guide treatment strategies in clinical LT. There have been minimal changes in the RAI since it was first introduced, with additional criteria for antibody-mediated rejection, a rare entity in LT, in 2016 (*6*). In parallel, options for induction and maintenance immunosuppression as well as treatments for biopsy-proven rejection episodes in LT have not changed substantially since the 1990s and rely on therapeutics that cause nonspecific suppression of entire leukocyte populations. For instance, the two mainstay treatments broadly suppress the T cell compartment [calcineurin inhibitors (CNIs)], or they function by globally inhibiting both macrophages and T cells (corticosteroids) (*7*). Thus, the absence of specific targeting for TCMR-associated immune subpopulations in LT results in both suboptimal prevention and treatment of TCMR episodes, as well as a variety of unintended, and often severe, adverse medication side effects.

Improving our understanding of the complex alloimmune microenvironment (AME) in clinical LT would enable development of focused and personalized immunotherapies, particularly as it relates to controlling the alloimmune response during rejection episodes. Donor-derived antigen-presenting cells (APCs) presenting allograft antigen on both major histocompatibility complex (MHC) I and II can activate host CD8$^+$ and CD4$^+$ T cells via the direct pathway, ultimately leading to tissue damage via Fas-FasL or granzyme/perforin production and secretion of pro-inflammatory cytokines (*8*). The indirect pathway, which has been implicated in late TCMR, is mediated by recipient APCs infiltrating the allograft over time (*8*). However, deeper characterization of graft-infiltrating leukocytes driving TCMR in clinical LT is still needed. When compared to experimental heart and kidney transplantation, small and large animal models of LT are more technically demanding while offering a lower threshold for tolerance induction and thus less opportunity to recapitulate alloimmunity in clinical TCMR (*9*). Moreover, most preclinical animal models focus on preventing alloimmunity at the time of transplant with resultant tolerance induction, rather than reversing a post-transplant rejection episode, which is the more common clinical scenario. Examination of clinical samples has been limited by the tiny amount of tissue available from a core needle biopsy specimen. The INTERLIVER study examined over 200 clinical LT biopsies using bulk tissue microarrays and archetypal analysis, and differentially expressed (DE) genes involving both effector T cell and injury-related pathways were identified in the small subset of biopsies with TCMR. Supervised and

[1]Division of Abdominal Organ Transplantation and Hepatobiliary Surgery, Department of Surgery, Keck School of Medicine, University of Southern California, Los Angeles, CA, USA. [2]Division of Biostatistics, Department of Population and Public Health, Keck School of Medicine, University of Southern California, Los Angeles, CA, USA. [3]Division of Gastroenterology, Hepatology and Nutrition, Children's Hospital Los Angeles, Los Angeles, CA, USA. [4]Department of Pathology, University of Southern California, Los Angeles, CA, USA. [5]Department of Anesthesiology, Perioperative and Pain Medicine, Stanford University School of Medicine, Stanford, CA, USA. [6]Department of Molecular Microbiology and Immunology, Keck School of Medicine, University of Southern California, Los Angeles, CA, USA. [7]Department of Medicine, Keck School of Medicine, University of Southern California, Los Angeles, CA, USA. [8]Division of Abdominal Organ Transplantation, Children's Hospital Los Angeles, Los Angeles, CA, USA.
*Corresponding author. Email: juliet.emamaullee@med.usc.edu
†These authors contributed equally to this work.

unsupervised molecular classifiers based on the top 30 DE genes had only a modest ability to predict histological TCMR [area under the curve (AUC) of 0.57 and 0.70, respectively] (*10*). A more recent histologic study analyzing post-LT biopsies demonstrated that $CD8^+$ T cells form an immune synapse with APCs, with an association between segregation of CD3- and CD45-positive cells, immunosuppression weaning failure, and development of TCMR (*11*). Thus, key features driving the intrahepatic alloimmune response during active rejection episodes, including composition and phenotype of alloreactive T cell subpopulations and interactions between innate and adaptive cells, remain elusive.

$CD4^+CD25^+FoxP3^+$ regulatory T cells (T_{regs}) have been a central focus in both experimental and clinical LT (*12*). Despite substantial evidence that T_{regs} are central mediators of rejection and immune tolerance, clinical trials designed to expand T_{reg} either via therapeutic intervention or cellular therapies have not yet resulted in positive clinical outcomes (*13*). The programmed death 1 (PD1) pathway has also emerged as an important physiologic immune checkpoint to maintain peripheral T cell tolerance and regulate adaptive immune responses particularly during chronic antigen exposure (*14*). PD1 can be expressed on both B and T cell populations, including T_{regs} upon activation, with constant high expression levels following sustained antigen exposure. The PD1 pathway antagonizes T cell receptor (TCR) engagement and CD28 costimulation signals, attenuating downstream cytokine production, proliferation, cell metabolism, and survival; thus, ultimately moderating T cell activity (*15*, *16*). The role of PD1 signaling in transplantation is not well defined, with preliminary studies on heart and kidney allografts implicating PD1-related signals as markers of allograft rejection (*17*–*22*). However, in a recent study in clinical LT, flow cytometric analysis failed to demonstrate a difference in PD1 expression in allograft-infiltrating T cells isolated from liver explant ($n = 5$), rejection ($n = 7$), and no-rejection liver biopsies ($n = 7$) (*23*). Thus, detailed study of the relationship between different regulatory and inflammatory immune cell populations is critical for defining the important aspects of the AME during rejection, optimizing identification of predictive biomarkers of TCMR, and identifying more focused targets for immunotherapy to treat active rejection.

Here, using multiplexed proteomics-based imaging mass cytometry (IMC), we developed a marker panel focused on immune cell phenotyping and developed an analysis pipeline that enabled granular, single-cell characterization of more than 30 discrete immune cell types, resulting in a spatially resolved, immune-focused single-cell atlas at a resolution that has not previously been achieved using this technique. This enabled spatial assessment of the AME in a large population of post-LT patients with no rejection (NR), active TCMR, and progression to chronic rejection (CR). We defined significant cell-cell interactions and identified spatial motifs as well as predicted single-cell phenotypes associated with active TCMR. This approach revealed that within the AME, the evolution of the immune response during active TCMR was associated with intragraft presence of specific T cell subpopulations expressing PD1. However, $PD1^+$ T cells were largely absent in CR, suggesting that these cells may reflect a natural attempt by the immune system to counteract the acute alloimmune inflammatory response and represent potential biomarkers unique to TCMR. In addition, the absence of these populations in CR might reflect failure of this immune regulatory mechanism in the setting of chronic alloimmunity. Furthermore, we showed that lymphocytes and macrophages are spatially organized into aggregates, in which strong interactions among $PD1^+$ and effector T cells exist, as well as between $CD8^+$ T cells and specific macrophage subpopulations. Collectively, our data offer a detailed and spatially conscious atlas of immune infiltrates in the liver AME during active TCMR episodes that represent putative in situ biomarkers of rejection. Our data provide a framework for histologic assessment of complex immune microenvironments at single-cell resolution in archival clinical samples, which can inform development of clinical assays improving treatment specificity and support the development of targets for immunotherapy to resolve clinical rejection episodes.

RESULTS

Part I: Major cell types and proportions in liver allografts during active rejection episodes

We applied IMC to 24 distinct NR liver core biopsies, 41 distinct biopsies with proven TCMR, and 14 distinct CR samples using our customized analysis pipeline (Fig. 1A). By segmenting the acquired 96 multiplexed images using clinically diagnostic regions of interest (ROIs) selected by a specialist liver pathologist, we generated a single-cell atlas of the AME containing a total of 461,816 cells (average 4811 ± 2291 cell per ROI), which were then classified into 10 main cell populations or "metaclusters." We evaluated raw image signals (fig. S1A), post-segmentation dimensionality reduction [t-distributed stochastic neighbor embedding (t-SNE)] of individual markers (fig. S1B), immune metaclusters by patient (fig. S1, C and D), and difference in mean fold change expression of all markers among the three clinical groups (fig. S1, E and F). We first projected metaclusters onto tissue sections, separating out non-immune metaclusters (hepatocytes, cholangiocytes, and endothelial cells) and immune metaclusters ($CD4^+$ T cells, $CD8^+$ T cells, macrophages, monocytes, neutrophils, B cells, and plasma cells) (Fig. 1B). We then quantified the number of cells within each metacluster and evaluated scaled marker expression of lineage markers (Fig. 1C). Hepatocytes were the most common non-immune cell type, representing 62.6% of all cells identified, while macrophages were the most common immune cell type, representing 9.9% of all cells identified. Rare populations were also identified, including cholangiocytes (1.8% of all cells) and B cells (1% of all cells). Next, t-SNE was used to visualize differences in cell metaclusters between clinical groups (Fig. 1D). Proportions of immune and non-immune populations were examined and compared between clinical groups. By looking at the expression of Ki67 and HLADR (human leukocyte antigen–DR) within non-immune cell populations, we identified three different subclusters of hepatocytes (fig. S2, A to D), cholangiocytes (fig. S2, F to I), and endothelial cells (fig. S2, K to O). Proliferating hepatocytes ($Ki67^+$ hepatocytes) and $HLADR^+$ hepatocytes presented a different distribution across the three groups, with a greater proportion of proliferating hepatocytes in TCMR ($P < 0.01$) and $HLADR^+$ hepatocytes in both TCMR and CR when compared to NR ($P < 0.01$) (fig. S2, D and E). Similarly, the percentage of $HLADR^+$ cholangiocytes differed across the three clinical groups, with a greater percentage of $HLADR^+$ cholangiocytes in both TCMR and CR compared to NR ($P = 0.01$; fig. S2, I and J). While MHC II molecules are constitutively expressed on human cholangiocytes, the inflammatory state of several diseases including primary biliary cirrhosis, primary sclerosing cholangitis, graft-versus-host disease, and even liver TCMR has been associated with MHC II overexpression on cholangiocytes, which may function as APCs in the liver (*24*, *25*).

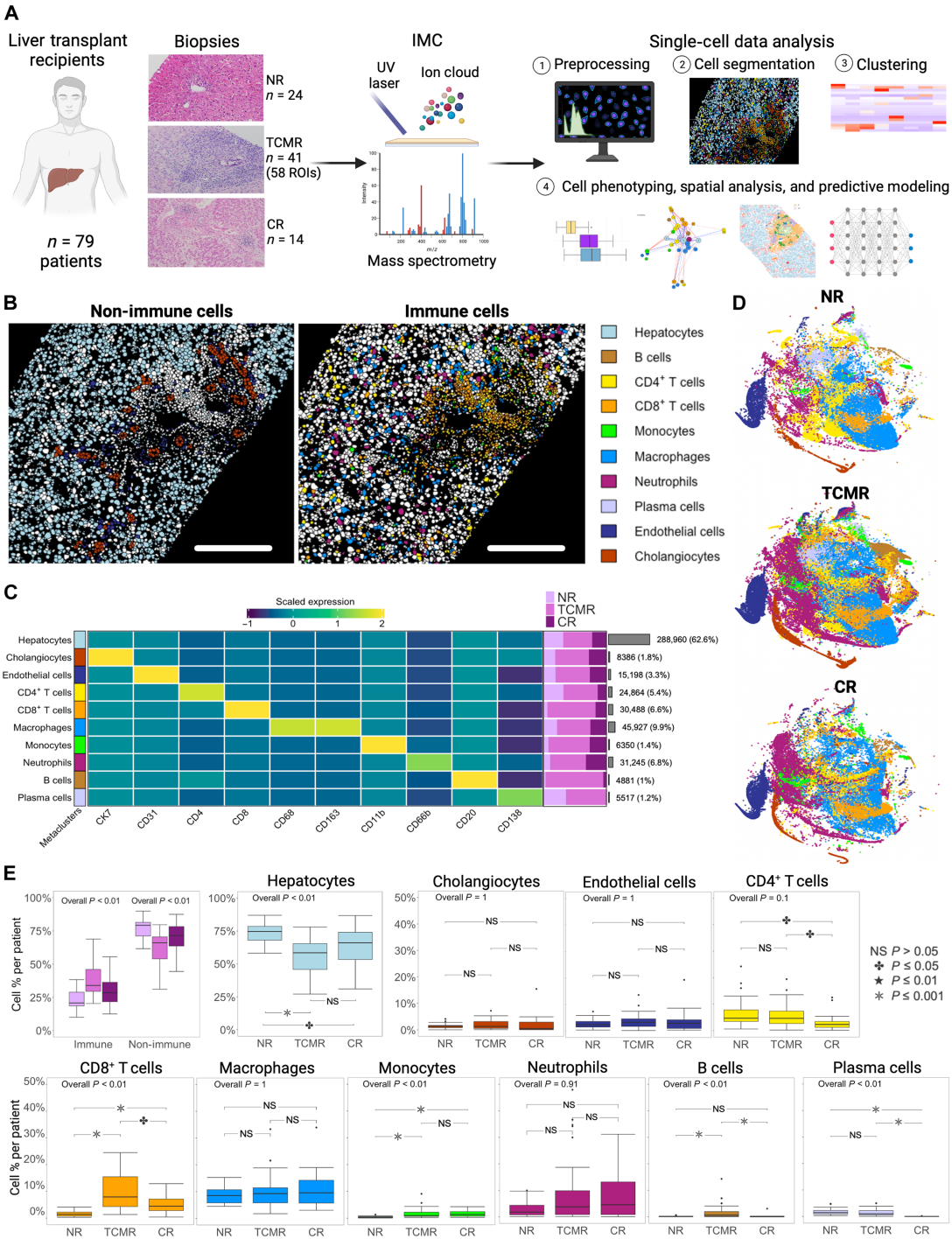

Fig. 1. Single-cell proteomic atlas of the global cellular composition in liver allografts using IMC. (**A**) Schematic figure of IMC workflow starting with case selection of biopsies including 96 specimens from 79 patients across clinical groups (NR, $n = 24$; T cell–mediated rejection, $n = 41$; and CR, $n = 14$). Tissue specimens were stained with our 22-marker IMC panel, and images were acquired. Images were preprocessed and segmented to generate masks and a single-cell expression matrix dataset. Downstream phenotypic analysis using a semi-supervised clustering approach and spatial analysis was performed on the dataset (461,816 cells). (**B**) Representative visualization of cell masks colored by cell population in non-immune and immune populations in TCMR. Scale bars, 190 μm. Cell population or metacluster colors from the legend are consistent throughout the figure. (**C**) Heatmap showing scaled marker expression within our 10 major metaclusters with purple bars with relative proportion of which clinical group contributed to the metacluster. Gray bars depict total cell number and percent composition of that population across the entire dataset. (**D**) t-SNE visualization showing cell metaclusters (excluding hepatocytes for ease of visualizing the less abundant metaclusters) by clinical group. (**E**) Boxplots representing the relative proportions of metaclusters across clinical groups with statistical comparison of each population as a proportion of that cell type per patient. TCMR and CR showed a greater proportion of immune cells compared to NR. Among the three clinical groups, different cell proportions were observed in $CD4^+$ and $CD8^+$ T cells, B cells, monocytes, and plasma cells compartments. UV, ultraviolet; *m/z*, mass/charge ratio; ROI, region of interest; NS, not significant.

Within immune metaclusters, there was an increase in $CD8^+$ T cells between NR and active TCMR as well as NR and CR ($P < 0.01$), with a subtle increase in monocytes from NR to TCMR ($P < 0.01$; Fig. 1E). Despite macrophages being the most common immune metacluster, which is consistent with their pivotal role in regulating liver immune function, there were no differences in abundance between clinical groups (Fig. 1E and fig. S1D) (*26*, *27*).

We performed a subanalysis on TCMR to determine whether demographics and immunosuppression history are correlated with cell-type proportions or not (table S1). Demographic variables analyzed were sex, race/ethnicity, and etiology. No difference was detected when analyzing metacluster cell proportions by demographics or immunosuppression history.

Evaluation of T cell and macrophage subpopulations in active TCMR shows expansion of exhausted phenotypes

Most antibodies available for use in IMC performed on human tissue were developed for studies related to cancer biology (*28*). After a comprehensive review, we developed a customized immune-focused IMC panel using a set of available markers able to holistically capture all the immune phenotypes involved in both inflammation and rejection pathophysiology (*28*). To uncover the various cell subpopulations and potentially important cell phenotypes within metaclusters, we then developed a semi-supervised clustering approach based on additional immune phenotype and functional markers within the $CD4^+$, $CD8^+$, B cell, macrophage, and monocyte immune metaclusters identified using multiplexed IMC.

$CD4^+$ T cells. Within the $CD4^+$ T cell compartment, nine total phenotypic subclusters were identified (Fig. 2, A to C, and fig. S3A). We initially stratified $CD4^+$ T cells by CD3 expression, resulting in a $CD3^{Low}CD4^+$ T cell subset and a $CD3^{High}CD4^+$ T cell subset. Variations in CD3 expression within the $CD4^+$ T cell compartment have been described, with low levels corresponding to resident memory $CD4^+$ T cells and high levels associated with an activated state (*29*, *30*). The resident memory $CD4^+$ T cell subset was more abundant in NR, while $CD3^{High}CD4^+$ T cells were more abundant in TCMR and CR (Fig. 2, D to F, and fig. S3, B and C). Compared to NR, active TCMR had a greater proportion of $CD3^{high}CD4^+$ T cells, naïve $CD4^+$ T cells, and activated $CD4^+$ T cells, which is consistent with acute alloreactivity (Fig. 2F). T_{regs} were identified as $CD3^+CD4^+FoxP3^+$ T cells (*31*). While their overall frequency was rare, we observed a concomitant increase in regulatory cell types, including $HLADR^+$ T_{regs} and $PD1^+CD4^+$ T cells, in the TCMR group when compared to NR, suggesting that their expansion counters effector alloreactive T cell activity (Fig. 2F). We also determined that the $CD3^{high}CD4^+$ T cell subset represented most of the $CD4^+$ T cells in CR, with a significant decrease in resident memory $CD4^+$ T cells and higher proportion of activated T cells when compared to NR (Fig. 2F). Unlike active TCMR, there was no expansion of the regulatory $HLADR^+$ T_{reg} or $PD1^+CD4^+$ T cell populations in CR. The frequency of these two cell populations was similar between NR and CR as well as between TCMR and CR. To understand the trajectory of $CD4^+$ T cells in the AME, pseudotime reconstruction was performed, which has been performed by other groups using IMC (Fig. 2G) (*32*–*35*). This provides further evidence that NR is primarily associated with resident memory $CD4^+$ T cells and suggests that $CD4^+$ T cell subpopulations increased during TCMR and CR originate and proliferate from circulating $CD4^+$ T cells (Fig. 2G). These data also suggest that the expanded T_{reg} and $PD1^+CD4+$ T cells observed in TCMR represent late-stage effector cells unique to this phase of alloimmunity.

$CD8^+$ T cells. Subclustering of the $CD8^+$ T cell compartment identified five unique $CD8^+$ T cell subsets, including $CD45^+CD3^+CD8^+$ ("$CD3^+CD8^+$ T cells"), $Ki67^+CD45^+CD3^+CD8^+$ ("proliferating $CD8^+$ T cells"), $GranzymeB^+CD45^+CD3^+CD8^+$ ("cytotoxic T cells"), $PD1^+CD45^+CD3^+CD8^+$ ("$PD1^+CD8^+$ T cells"), and $PD1^+CD28^+CD45^+CD3^+CD8^+$ ("$PD1^+CD28^+CD8^+$ T cells") (Fig. 3, A to C, and fig. S3D). Although the overall $CD8^+$ T cell proportion differed between clinical groups (Fig. 1E), the $CD3^+CD8^+$ T cell subgroup was the most abundant subset in each patient and across each cohort (Fig. 3, D and E). Active TCMR showed a higher overall frequency of $CD8^+$ T cells when compared to both NR and CR ($P < 0.01$; Fig. 1E), and this was predominately related to an increased frequency of proliferating $CD8^+$ T cells, supporting the concept of effector $CD8^+$ T cell expansion during acute alloimmunity (Fig. 3, D to F). Cytotoxic T cells were rare and showed no differences across clinical groups within the $CD8^+$ T cell compartment (Fig. 3F). Similar to what was observed for $CD4^+$ T cells, TCMR tissue exhibited a greater enrichment of $PD1^+CD8^+$ T cells when compared to NR and CR ($P < 0.05$) (Fig. 3F). Pseudotime analysis to evaluate $CD8^+$ T cell trajectory revealed two divergent paths of the abundant $CD3^+CD8^+$ T cells, into either the $PD1^+$ phenotype or the $Ki67^+$ proliferating $CD8^+$ phenotype (Fig. 3G). This suggests that this population has its own terminally differentiated function including counteract the alloimmune inflammatory response in the attempt to restore the homeostasis.

Macrophages. Among the immune metaclusters, macrophages were the most abundant cell type (fig. S1D) in all clinical groups, which highlights their key role in liver homeostasis, disease, and injury processes (*26*, *27*). Macrophages can participate in robust infiltration of the AME during severe rejection episodes; however, their role has rarely been investigated in TCMR and CR in clinical LT (*36*, *37*). We have previously shown that CR is characterized by a discrete macrophage phenotype absent in NR (*37*). Thus, to obtain a detailed representation of the macrophages complexity and heterogenous activity in LT, we first divided macrophages M1 and M2 based on their expression of CD163 (fig. S4A) (*38*). We were not able to identify a discrete protein marker for Kupffer cells, which limited our ability to further differentiate these tissue specific macrophages within our macrophage metacluster. The overall distribution of M1 and M2 and ratio of M2:M1 macrophages did not differ between NR, active TCMR, and CR (fig. S4, B to D) (*38*). Even when classified into M1 and M2 phenotypes, macrophages remain extremely plastic in vivo, and the role of different subsets of activated M2 macrophages in solid organ transplantation is yet to be fully understood (*39*). In addition, it has been described that M2 macrophages are crucial in the development of chronic allograft rejection promoting allograft fibrosis and chronic allograft vasculopathy in heart and kidney transplants (*40*, *41*). Thus, we sought to further characterize these two macrophages population and relate them to the three different alloreactive states. Subclustering revealed four M1 ["M1" ($CD68^+CD163^{Lo}$), "$CD11b^+$ M1" ($CD11b^+CD68^+CD163^{Lo}$), $CD16^+$ M1 ($CD16^+CD68^+CD163^{Lo}$), and "proliferating M1" ($Ki67^+CD68^+CD163^{Lo}$)] and five M2 macrophage subtypes ["M2" ($CD68^+CD163^{Hi}$), "$CD11b^+$M2" ($CD11b^+CD68^+CD163^{Hi}$), $CD16^+$ M2 ($CD16^+CD68^+CD163^{Hi}$), "proliferating M2" ($Ki67^+CD68^+CD163^{Hi}$), and "$HLADR^+$ M2" ($HLADR^+CD68^+CD163^{Hi}$); Fig. 4, A to C, and fig. S4E]. Consistent with the activation of an inflammatory process, a greater percentage of proliferating M1 macrophages was observed in TCMR compared to NR and CR (Fig. 4F). We found one M1 and one M2 macrophage subset each expressing CD16, which has been associated with heart transplant rejection (*40*). Both NR and

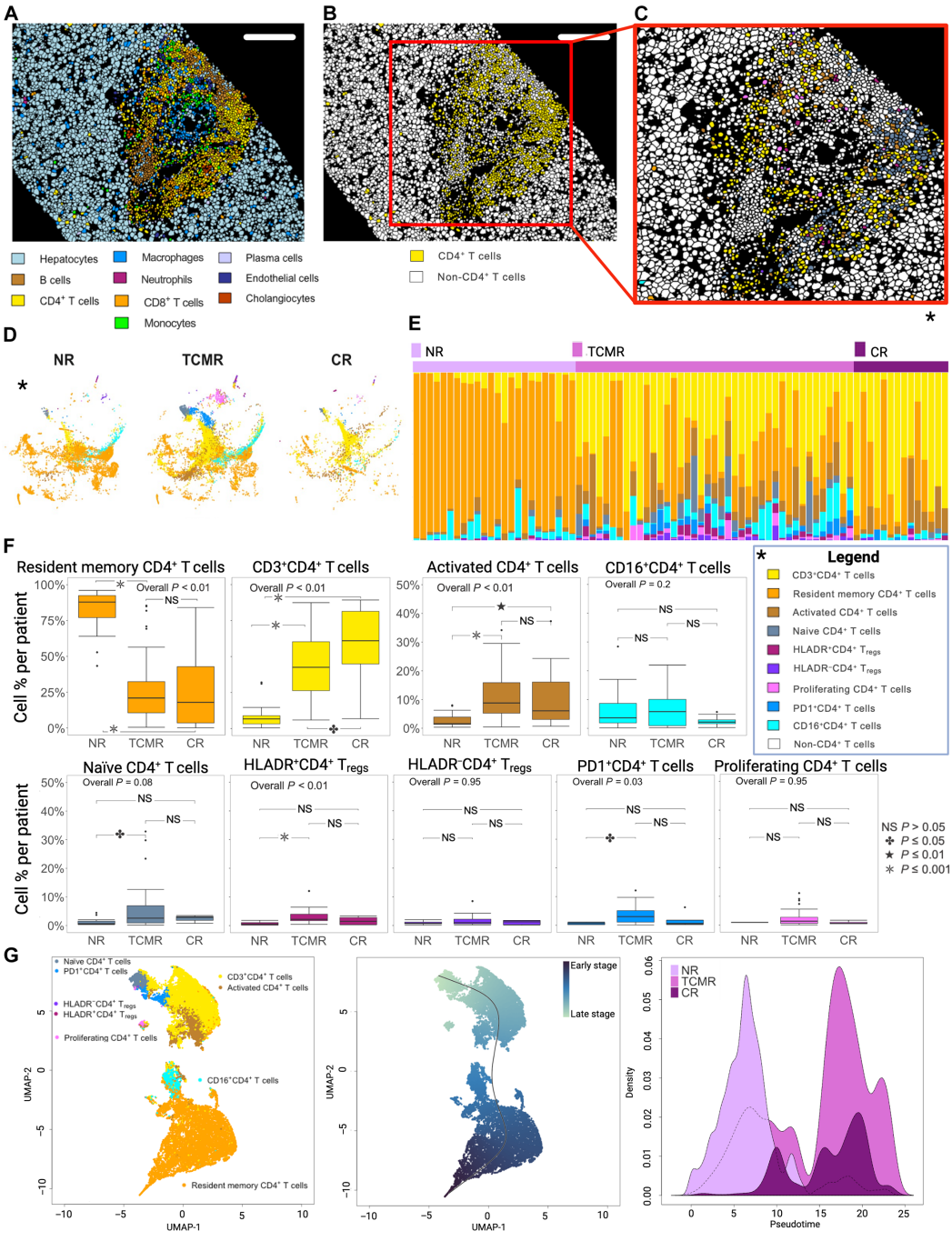

Fig. 2. Active TCMR is uniquely characterized by expansion of T_{reg} and PD1$^+$CD4$^+$ T cells. (**A**) Visualization of cell masks colored by metaclusters on representative TCMR tissue section. Scale bar, 180 μm. (**B**) Plot of the same TCMR tissue section with yellow coloring indicating location of CD4$^+$ T cells within the representative core biopsy. Scale bar, 180 μm. (**C**) Zoom panel highlighting CD4$^+$ T cells colored by cell subpopulation (see color key legend). Subpopulations were identified using unsupervised clustering within the CD4$^+$ T cell metacluster, which comprised 24,864 cells, using expression values from markers CD28, CD16, CD11b, CD45, CD4, PD1, FoxP3, Ki67, CD3, and HLADR. Nine unique subpopulations emerged from this analysis: Resident memory CD4$^+$ T cells, CD3$^+$CD4$^+$ T cells, activated (HLADR^{hi}) CD4$^+$ T cells, CD16$^+$CD4$^+$ T cells, naïve CD4$^+$ T cells, HLADR$^+$CD4$^+$ T_{regs}, HLADR$^-$CD4$^+$ T_{regs}, PD1$^+$CD4$^+$ T cells, and proliferating (Ki67$^+$) CD4$^+$ T cells. (**D**) tSNE visualizations showing CD4$^+$ T cell subpopulations by clinical group. (**E**) Stacked bar plot representing cell subpopulation proportions within individual patients by clinical group. (**F**) Boxplots showing CD4$^+$ cell subpopulation percent per patient as a fraction of the CD4$^+$ T cell population. Resident memory CD4$^+$ T cells represented the most abundant phenotype observed in NR ($P < 0.01$); CD3$^+$CD4$^+$ T cells were the predominant phenotype detected in both TCMR and CR groups ($P < 0.01$), which presented a greater proportion of activated CD4$^+$ T cells for both versus NR ($P < 0.01$); TCMR showed a greater proportion of naïve CD4$^+$ and PD1$^+$ T cells ($P = 0.03$) as well as HLADR$^+$ T_{regs} ($P < 0.01$) compared to NR. (**G**) Pseudotemporal trajectory analysis of the CD4$^+$ compartment with uniform manifold approximation and projection (UMAP) of cell populations. The leftmost panel shows UMAP plot with cell subpopulations, and second panel shows the predicted temporal trajectory (black line, bottom to top). The rightmost panel depicts the density of CD4$^+$ T cells (*y* axis) from each clinical group across pseudotime (*x* axis). PD1$^+$CD4$^+$ T cells and T_{regs} represent late-stage effector CD4$^+$ populations specific to TCMR.

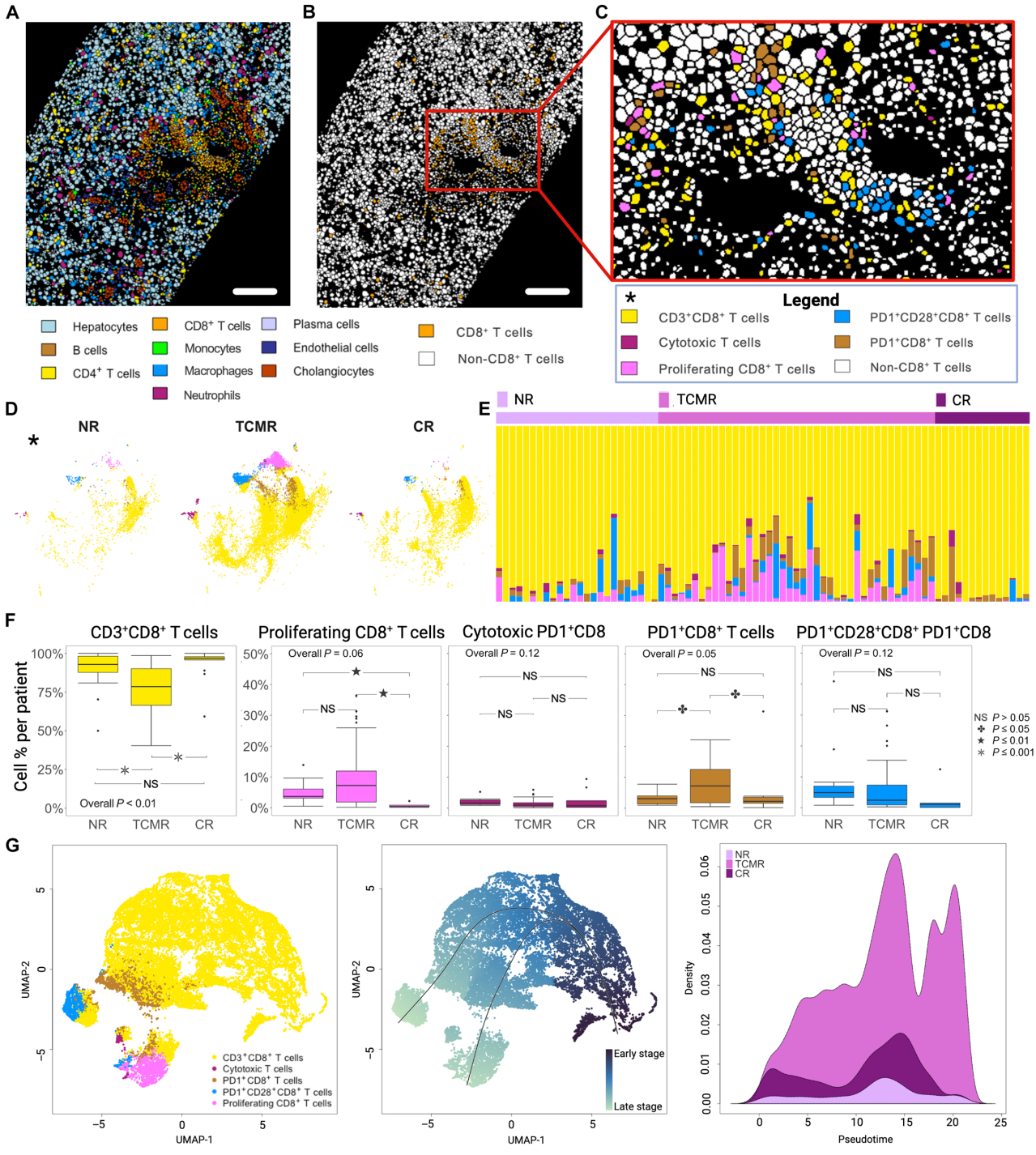

Fig. 3. CD8$^+$ T cell profile in active TCMR highlights simultaneous increases in cell proliferation and PD1$^+$ subpopulations. (**A**) Representative TCMR image with metaclusters projected onto the mask outline of core biopsy ROI. Scale bar, 190 μm. (**B**) TCMR mask image now highlighting CD8$^+$ T cells only in orange. Scale bar, 190 μm. (**C**) Zoom panel of CD8$^+$ T cells colored by cell subpopulation (see color key). Similar as with CD4$^+$ T cells, the CD8$^+$ compartment was categorized into subpopulations using unsupervised clustering with the following markers: CD28, CD16, CD11b, CD45, CD8, PD1, FoxP3, Ki67, CD3, HLADR, and Granzyme B. Five unique subpopulations were identified from the parent CD8$^+$ population comprising 30,488 total cells: CD3$^+$CD8$^+$ T cells, proliferating (Ki67$^+$) T cells, cytotoxic T cells, PD1$^+$CD8$^+$ T cells, and PD1$^+$CD28$^+$ T cells. (**D**) tSNE of CD8$^+$ T cell subpopulations. (**E**) Stacked bar plot showing individual CD8$^+$ T cell subpopulations by patient and clinical group. (**F**) Boxplots depicting CD8$^+$ T cell subpopulations as a percent of total CD8$^+$ T cell population and compared across clinical group. Different distribution in CD3$^+$CD8$^+$ T cells, proliferating, and PD1$^+$CD8$^+$ T cells subpopulation was observed across the three clinical groups, with a greater proportion of proliferating and PD1$^+$CD8$^+$ T cells in TCMR. (**G**) Leftmost panel with pseudotime UMAP plot of CD8$^+$ T cell subpopulations and middle panel showing dual trajectory starting at the darker portion of the graph and moving to the lower left of the plot. Plot of density of CD8$^+$ T cells (*y* axis) in each clinical group across pseudotime (*x* axis). Stimulation of CD3$^+$CD8$^+$ T cells results in the maturation of two distinct phenotypes represented by a proliferating CD8$^+$ T cells and a distinct PD1$^+$CD8$^+$ T cell subpopulation.

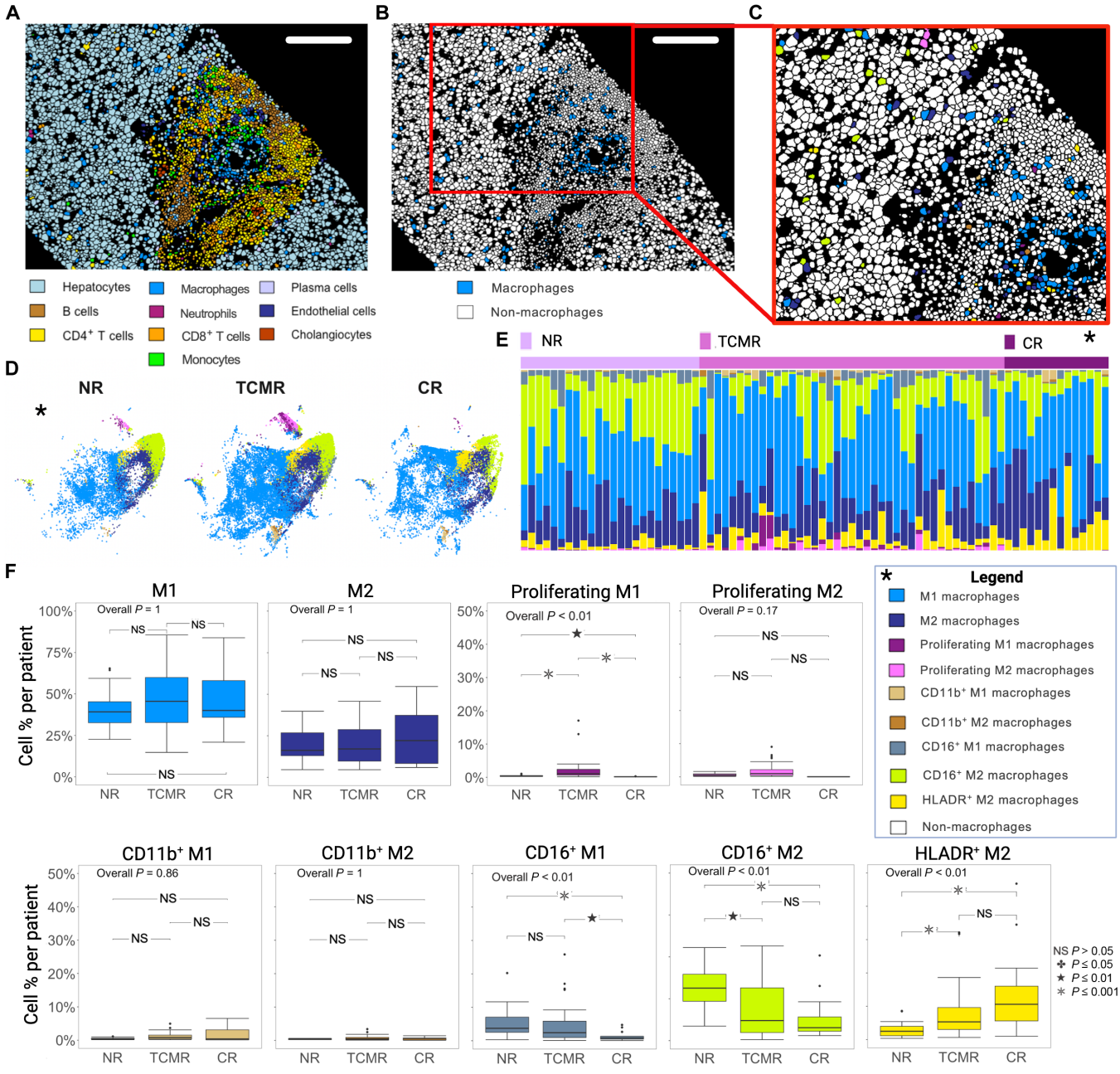

Fig. 4. Both active TCMR and CR are characterized by increased proportion of HLADR$^+$ M2 macrophages with concurrent decreases in CD16$^+$ M1 and M2 macrophages. (**A**) Cell mask visualization on TCMR tissue section colored by metacluster. Scale bar, 190 μm. (**B**) TCMR tissue section again with cell mask outlines and colored blue to show location of the macrophage metacluster cells within the tissue. Scale bar, 190 μm. (**C**) Zoom panel of macrophage subpopulations (see color key legend). The macrophage metacluster was composed of 45,927 total cells within the entire dataset, and subpopulations were identified by first differentiating M1 (CD163^{Lo}) from M2 (CD163^{hi}) and then performing unsupervised clustering based on expression of CD16, CD11b, CD45, FoxP3, CD163, CD68, Ki67, and HLADR. Nine distinct subpopulations emerged from this analysis including generic M1 and M2 populations, proliferating (Ki67$^+$) M1 macrophages, proliferating (Ki67$^+$) M2 macrophages, CD11b$^+$ M1 macrophages, CD11b$^+$ M2 macrophages, CD16$^+$ M1 macrophages, CD16$^+$ M2 macrophages, and HLADR$^+$ M2 macrophages. (**D**) tSNE plot of macrophage subpopulations separated by clinical group. (**E**) Stacked bar plot of individual macrophage subpopulations by patient and clinical group. (**F**) Boxplots showing macrophage subpopulations as a percent of the overall macrophage population per patient. A greater proportion of proliferating M1 macrophages was observed in TCMR compared to NR and CR; TCMR and NR had a greater proportion of CD16$^+$ M1 macrophages compared to CR; NR showed a greater cell percentage of CD16$^+$ M2 macrophages compared to TCMR and CR; HLADR$^+$ M2 macrophages were more abundant in both TCMR and CR compared to NR.

TCMR exhibited a greater percentage of $CD16^+$ M1 macrophages when compared with CR ($P < 0.01$; Fig. 4F). The $CD16^+$ M2 macrophage subcluster was most abundant in NR and was progressively depleted from TCMR to CR ($P < 0.01$; Fig. 4F). These cells might represent a population of regulatory and anti-inflammatory macrophages (M2b), capable of interleukin-10 (IL-10) secretion (Fig. 4F) (*42*, *43*). A subpopulation of $HLADR^+$ M2 macrophages showed the opposing pattern to $CD16^+$ M2 cells and was more abundant in both TCMR and CR than NR ($P < 0.01$; Fig. 4F). These $HLADR^+$ M2 macrophages might represent a different activation state compared with the generic M2 macrophage subpopulations or suggest a unique specialization of those cells such as for antigen presentation.

Monocytes. Within the monocyte metacluster, which represented 1.4% of all cells identified, we defined four phenotypes: classical ($CD11b^+CD16^+$), nonclassical ($CD11b^+CD16^-$), intermediate ($CD11b^+CD16^+HLADR^+$), and activated monocytes ($CD11b^+CD16^-HLADR^+$) (fig. S5, A to D). Classical monocytes represented the most abundant subset across all clinical groups (fig. S5, E and F), and the comparison of percentage across the three clinical groups showed that intermediate monocytes comprised a greater proportion of the monocyte metacluster in NR compared with TCMR and CR ($P < 0.01$; fig. S5G).

B cells and plasma cells. B cells represented the smallest metacluster in the overall dataset (4881 or 1% of all cells identified; Fig. 1C). Comparison of three B cell subpopulations identified (B cells, $PD1^+$ B cells, and proliferating B cells) did not highlight any difference in the frequency of $PD1^+$ B cells and proliferating B cells across clinical groups (fig. S6G). Last, the small fraction of plasma cells identified, representing 1.2% of all cells in the dataset, showed a higher proportion in TCMR than CR ($P < 0.01$; Fig. 1E).

Part II: Evaluation of spatial relationships and multicellular functional motifs that define specific pathogenic immune cell subsets involved in active TCMR and CR

First, we examined the spatial data layer from our single-cell proteomic IMC atlas of liver transplant alloimmunity to assess pairwise relationships between discrete immune subpopulations within each clinical group using both neighborhood and correlation analysis to characterize the statistical probabilities of cell-to-cell interactions (Fig. 5). Overall, a greater number of significant cellular interactions, either via avoidance or attraction, were observed in TCMR when compared to NR and CR (Fig. 5, A to D). The AME in active TCMR was characterized by $CD3^+CD8^+$ T cells showing attraction to APCs including proliferating and M1 macrophages, classical monocytes, $HLADR^+$ M2 macrophages, and B cells, as well as $CD3^+CD4^+$ T cells, supporting the concept of complex multicellular interactions characterizing this pro-inflammatory state (Fig. 5C). Neighborhood analysis revealed the presence of $PD1^+$ T cells ($PD1^+CD4^+$, $PD1^+CD28^+CD8^+$, and $PD1^+CD8^+$ T cells) and T_{regs} in the vicinity of effector T cells, which established a greater number of positive interactions when compared to NR, suggesting that a close cross-talk between those two ends of the spectrum T cell phenotypes occurs in TCMR (Fig. 5, A and C). Conversely, resident memory $CD4^+$ T cells showed no contact or avoidance with exhausted phenotypes in NR and TCMR, respectively (Fig. 5, A to C). In CR, $HLADR^+$ M2 macrophages surrounded $HLADR^+$ hepatocytes and M1 macrophages, while reciprocal strong interaction between $CD16^+$ M2 macrophages and M2 macrophages was observed, likely representing a niche in which further differentiation of M2 macrophages occurs (Fig. 5D). These results are not affected by cell-type abundance. The greater presence of a particular cell type does not necessarily correlate to that cell type having a greater chance of interacting with other cell types. Hepatocytes, the most abundant cell type, showed a strong avoidance with most other cell types, regardless of clinical group. On the other hand, cytotoxic T cells (cluster 21) and $PD1^+CD28^+CD8^+$ T cells (cluster 23) showed an increase in interaction strength in TCMR despite being somewhat less abundant compared to NR.

Because of the relationship of the RAI score for TCMR to endothelial inflammation, we evaluated the distributions of distance to endothelial cells and each immune subpopulation across clinical groups (Fig. 5E). Most pro-inflammatory subpopulations including $CD3^+CD4^+$ and $CD3^+CD8^+$ T cells, proliferating and cytotoxic $CD8^+$ T cells, and classical monocytes resided near $CD31^+$ endothelial cells, while resident memory $CD4^+$ T cells, $CD16^+$ M1 macrophages, and $CD16^+$ M2 macrophages were distributed throughout the tissue (Fig. 5E). Looking at TCMR alone, we sought to analyze how RAI score and subscores may affect cell proportion differences and spatial distribution. Despite observing heterogeneity in the RAI score and its various subscores across patients (fig. S7, A to D), we observed no difference in metacluster cell proportion ($P > 0.05$). Looking at subcluster cell proportions, the only significant difference was found when comparing the cholangiocyte subcluster ($P = 0.03$), stratified by venous score. No differences were found when comparing $CD4^+$ T cell, $CD8^+$ T cell, macrophage, monocyte, B cell, hepatocyte, endothelial cell, and the remaining cholangiocyte subcluster cell proportions ($P > 0.05$). When evaluating the distribution of distance to endothelial cells and each immune subpopulation, we observe no visual difference across RAI score and portal score (fig. S7, E and F). These outputs correlate with our neighborhood analysis, in which we observe no significant differences in these structural markers across clinical group (Fig. 5C).

To evaluate higher-order spatial motifs as potential functional units associated with liver allograft pathology, we performed cellular neighborhood (CN) analysis (*44*, *45*). Cells were clustered into nine CNs (Fig. 6) based on aggregated values of their 10 nearest neighboring cells. These CNs represent spatial structures formed by cells and their spatial relationship to neighboring cells. These were labeled according to the unique cell types in each cluster as shown in the heatmap in Fig. 6A: hepatocytes, vasculature, granulocyte enriched, activated macrophages, CD8 enriched, $CD16^+$ T helper enriched, T helper enriched, B cell and monocyte enriched, and bile ducts (Fig. 6, A to C). We then visualized and compared the proportions of these CNs across clinical groups (Fig. 6, B to D). For the non-immune predominant CNs (hepatocyte, vascular, and bile duct), there were few differences between clinical groups except for a slightly smaller proportion of the hepatocyte CN in TCMR (likely a direct consequence of the increase of immune cell enriched CNs in TCMR; Fig. 6D). The CD8-enriched CN (which included $HLADR^+$ T_{reg} and both $PD1^+CD8^+$ T cell subpopulations) was expanded in active TCMR when compared with NR and CR ($P < 0.001$ and $P < 0.01$, respectively). In addition, the "B cell and monocyte" CN was most abundant in TCMR and was also expanded in CR compared to NR ($P < 0.001$). Conversely, the $CD16^+$ T helper–enriched CN was more abundant in NR when compared with TCMR and CR ($P < 0.001$), suggesting that this CN could be a marker of allograft tissue homeostasis (Fig. 6D).

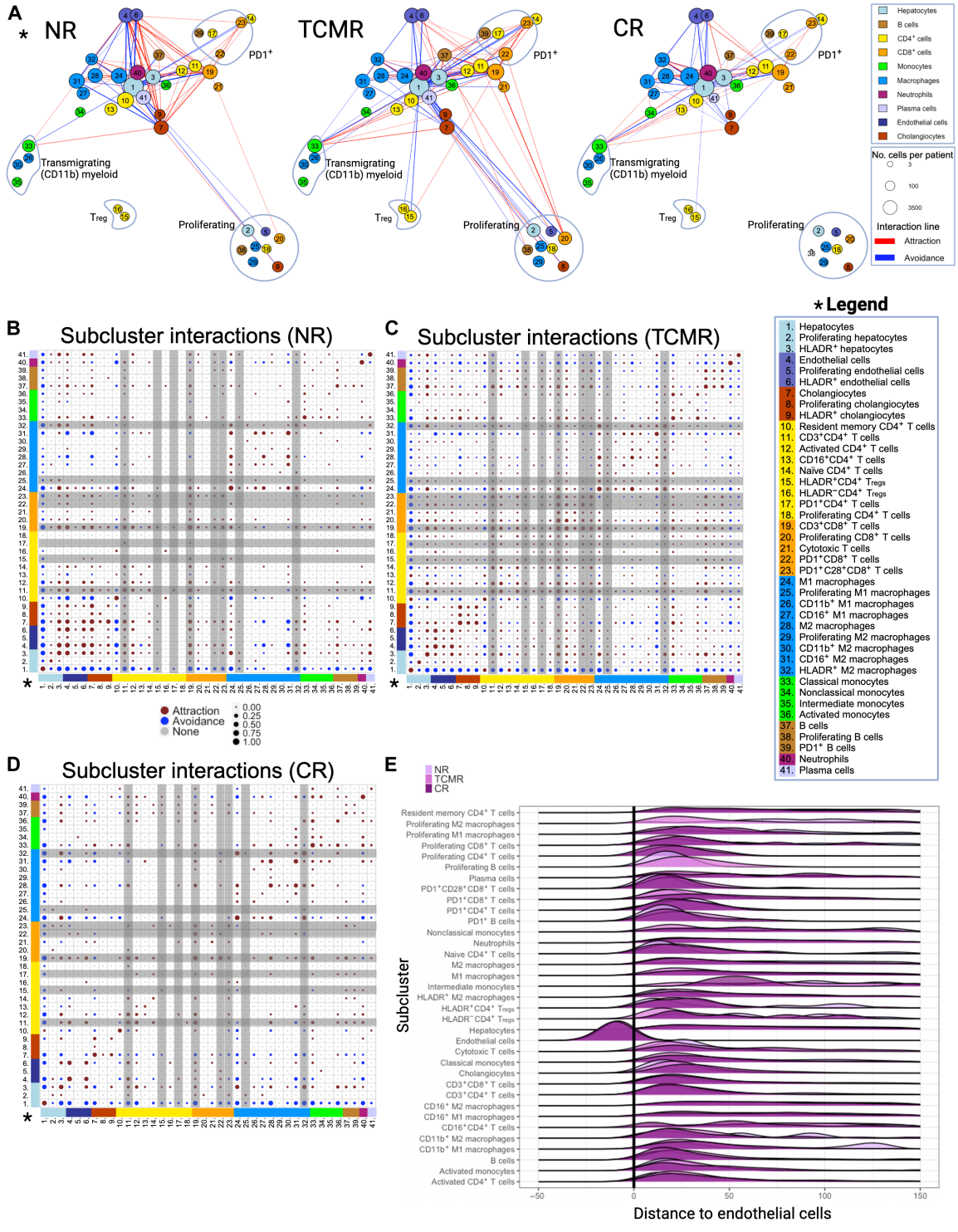

Fig. 5. Spatial relationship analysis between immune cell subsets across clinical groups shows increased interactions in exhaustion phenotype (T_{reg}, $PD1^+$, leukocytes) and proliferating cell types in active TCMR. (**A**) Spatial correlation network visualization showing attractions (red line) and avoidances (blue line) across cell subpopulations and colored by the metacluster that the subpopulation is derived from. The line thickness represents the strength of the degree of attraction, or avoidance between the cell subpopulations and the size of the circle represents the size of the subpopulation. For ease of visualization, the $CD11b^+$ monocyte/macrophage, $PD1^+$, proliferating, and T_{reg} populations are grouped in phenotype clusters (gray circle highlights). Lymphocytes exhibiting an exhausted phenotype (clusters number 17, 22, 23, and 39) showed a greater number of interactions in TCMR compared to NR and CR. (**B** to **D**) Heatmap showing pairwise spatial interaction between subclusters in NR (B), TCMR (C), and CR (D). (**E**) Plot of spatial distance of subcluster populations to endothelium.

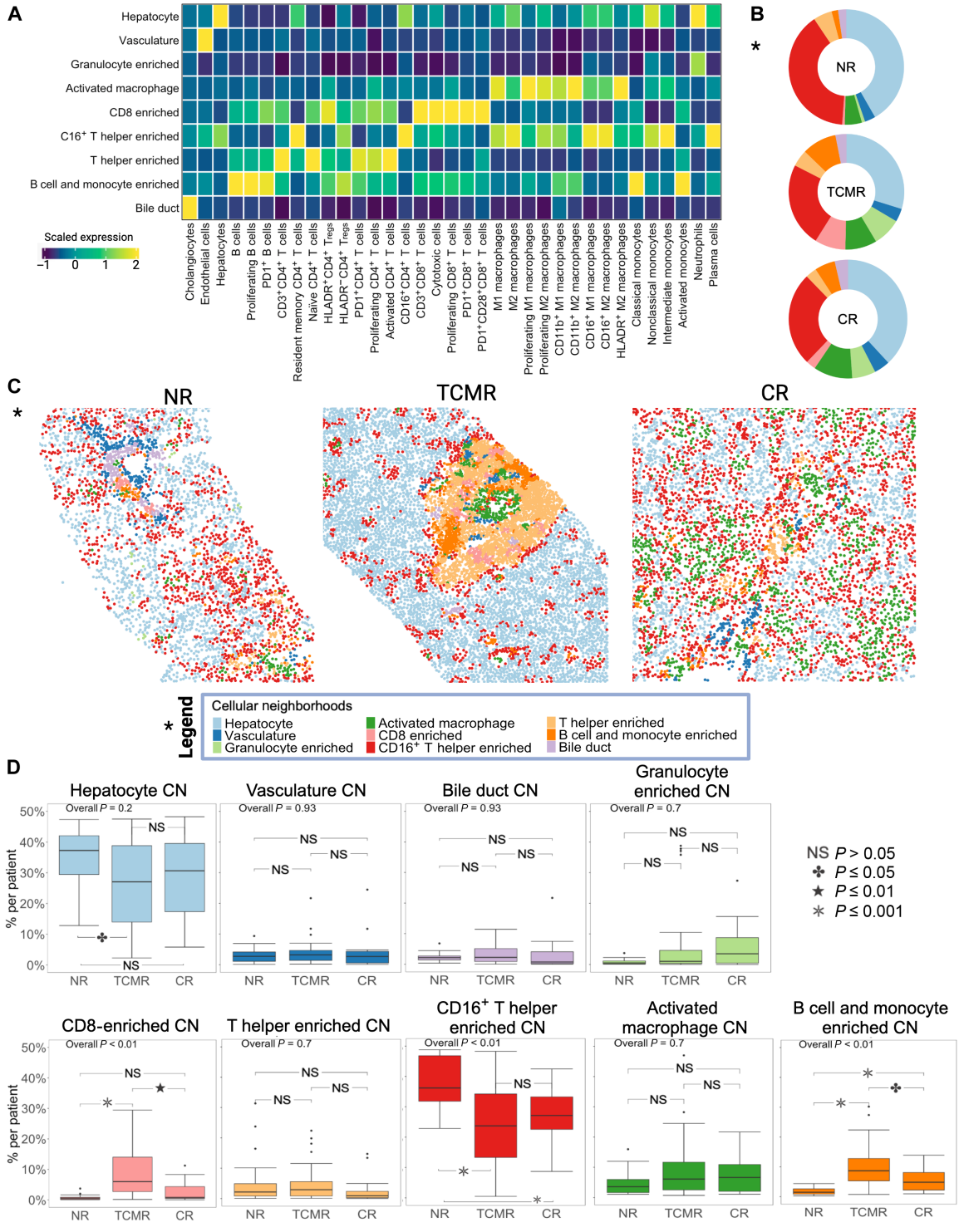

Fig. 6. Spatial profiling of liver allograft biopsies uncovers eight higher-order CN motifs that are differentially abundant across clinical groups, including a unique CD8-enriched CN containing exhaustion phenotype subsets that is strongly associated with active TCMR. (**A**) Heatmap showing composition of CN clusters. From the 35 identified cell populations and subpopulations in our dataset, we obtained nine distinct CNs or spatial motifs that are found within our dataset which include: Hepatocyte, vasculature, granulocyte enriched, activated macrophages, CD8 enriched, CD16$^+$ T helper enriched, T helper enriched, B cell and monocyte enriched, and bile duct. (**B**) Donut plots showing proportions of CNs by clinical group. TCMR has the largest proportion of CD8 enriched and B cell and monocyte enriched CNs. NR has the proportion of CD16$^+$ T helper–enriched CN. (**C**) Visualization of CNs projected onto representative biopsy specimens from NR, TCMR, and CR. (**D**) Boxplots depicting the percent makeup of CNs compared between clinical groups. Difference in percentage distribution was reported for CD8 enriched, which presented a greater percentage in TCMR compared to NR and CR; CD16 T helper–enriched CN presented a higher percentage in NR compared to TCMR and CR, and no difference was observed between TCMR and NR; the percentage of B cell and monocytes enriched CN was higher in TCMR compared to NR and CR, while CR showed a greater proportion compared to NR.

Part III: Confirmation of presence of exhaustion markers in liver AME during active TCMR using bulk RNA sequencing

Our single-cell atlas across the spectrum of rejection in LT identified several unique cell types increased during active TCMR, including T_{regs}, $PD1^+CD4^+$ T cells, $PD1^+CD8^+$ T cells, and $HLADR^+$ M2 macrophages. To confirm the presence of cells with this phenotype and obtain further evidence about their functional status, including whether the identified $PD1^+$ T cells represent a terminally differentiated, activated $CD4^+$ or $CD8^+$ T cell versus an exhausted effector T cell population, we performed bulk transcriptomic analysis on subsequent sections of formalin-fixed paraffin-embedded (FFPE) biopsies using the nCounter platform (*46*). Eight samples, comprising the most representative four TCMR and four NR cases based on cellular composition in IMC, were selected for this analysis. A group of 23 genes defining T cell phenotypes including helper function, exhaustion, and cytotoxic activity are highlighted in Fig. 7A. By comparing DE genes between NR and TCMR, we identified an overall up-regulation of genes typically associated with cytotoxic activity as well as up-regulation of *PDCD1* (programmed cell death 1 or PD1) gene expression in TCMR samples, which is consistent with the higher percentage of $PD1^+CD4^+$ and $CD8^+$ T cells identified in our IMC dataset (Fig. 7A). We also observed increased DE of *PDCD1LG1* (Programmed cell death-ligand 1 or PD-L1), *PDCD1LG2*, *CTLA4* (cytotoxic T-lymphocyte–associated protein 4), *LAG3* (lymphocyte activating 3), and *CD160* (CD160 antigen) genes in TCMR compared to NR, confirming up-regulation of both ligands for PD1 and other T cell exhaustion markers (Fig. 7A). A group of 18 genes which differentiate the diverse macrophage polarization in M1, M2a, M2b, and M2c are shown in the heatmap in Fig. 7B. Genes for both pro-inflammatory cytokines such as *CXCL9* and *CXCL10*, mainly expressed by M1 macrophages, and anti-inflammatory cytokines including *IL-10*, *CCL22* (C-C motif chemokine ligand 22), and *CCL24,* mostly associated with M2 macrophage polarization, were up-regulated in active TCMR when compared to NR. We have not yet identified a reliable natural killer (NK) marker for IMC in liver tissue, so we evaluated markers of NK cells including *IL21R* (interleukin 21 receptor), *XCL1* (X-C motif chemokine ligand 1), and *NCR1* (natural cytotoxicity triggering receptor 1), which were up-regulated in TCMR samples (Fig. 7B). We also identified an overall up-regulation of several genes associated with neutrophils, B cells, mast cells, and dendritic cells (fig. S8A). Because we performed our analysis on a subset of cases from our IMC cohorts, we sought to validate these results using publicly available data that includes six cases of biopsy-proven active TCMR in clinical LT (*31*). This confirmed our bulk RNA sequencing (RNA-seq) analysis, demonstrating similar up-regulation of DE genes (fig. S8B). After observing that $PD1^+$ T cell expansion in active TCMR was supported by both IMC (proteomic) and RNA-seq assays, we have begun to expand our IMC panel with inclusion of both ligands for PD1, PDL1, and PDL2 (Fig. 7C). A pilot experiment performed on three representative cases of active TCMR and NR confirmed expression of PDL1 and PDL2 at a protein level on the surface of both M1 and M2 macrophages (Fig. 7C). In addition, both $PD1^+CD4^+$ and $CD8^+$ T cells were proximal to macrophages expressing either PDL1 or PDL2, suggesting a close interaction among those immune phenotypes and a key role for PD1 pathway in the mechanism of active TCMR (Fig. 7C, right).

Part IV: Use of machine learning techniques to select which cell types in the AME are most strongly associated with active TCMR to guide biomarker and therapeutic target development

The analysis of the AME in NR, active TCMR, and CR identified 41 potential features of which 14 immune and 5 non-immune differed in patients who developed TCMR from NR, 9 immune and 4 non-immune features distinguished TCMR from CR, and 10 immune and 1 non-immune features separated out NR from CR, thereby highlighting complex network of different cell phenotypes specific for those three AMEs. To determine whether these immune phenotypes could predict patient outcomes, LASSO (least absolute shrinkage and selection operator) regression was applied to the entire dataset. To improve model robustness, fivefold cross-validation (CV) was used to determine model parameters, and a 5000 iterative bootstrapping technique was used to perform feature selection by determining feature importance based on frequency. To ensure that predicted results and model performance are derived from patients not included when training the model, internal CV was performed using repeated random subsampling (1000 iterations of randomly splitting the data into training and validation sets); performance metrics were averaged, and the median prediction of each patient was used for further model evaluation. Examination of the most important features, which present a frequency $\geq 50\%$, revealed that eight cell subpopulations contributed the most in generating a model that can accurately differentiate active TCMR versus NR (means $\pm$ SD; accuracy of 0.89 ± 0.07 and AUC of 0.96 ± 0.04), demonstrating a high correlation between median prediction and actual clinical outcome (Spearman correlation coefficient $R = 0.77$, $P = 7.206 \times 10^{-10}$) (Fig. 8, A to C, and fig. S9A). The highest-ranking immune phenotype was resident memory $CD4^+$ T cells, which was a predictor of NR, corresponding to pairwise analysis and thus demonstrating that this immune subset was strongly associated with NR (as shown in Fig. 2). In addition, intermediate monocytes, cholangiocytes, and $CD16^+$ M2 macrophages were predictors of NR. On the other hand, $PD1^+CD4^+$ T cells, $HLADR^+$ M2 macrophages, nonclassical monocytes, and proliferating hepatocytes were positive predictors of active TCMR (Fig. 8B). Application of this modeling approach to differentiate TCMR from CR resulted in nine highly ranked features that can accurately distinguish these two alloimmune states, with a high sensitivity, specificity, and accuracy, and a mean AUC of 0.96 ± 0.04 (Spearman correlation coefficient between prediction and actual outcome of 0.82, $P = 1.782 \times 10^{-9}$) (Fig. 8, D and F). Among these features, proliferating and $CD16^+$ M1 macrophages, proliferating and $PD1^+$ $CD8^+$ T cells, plasma cells, and $CD3^+$ and $CD16^+$ $CD4^+$ T cells predicted TCMR, while the $CD3^+CD8^+$ T cell phenotype was a predictor of CR (Fig. 8E and fig. S9B). Modeling for differentiating NR from CR was also highly sensitive and specific; however, the sample size for this comparison (38 samples total) may be too small to generate a conclusion (fig. S9). Overall, these results indicate that rare but specific cell subpopulations identified in the present study potentially harbor high value as biomarker and therapeutic targets to treat active TCMR and CR in clinical LT.

DISCUSSION

Our study provides a comprehensive single-cell, spatially resolved analysis of the AME in clinical LT, revealing the complexity of alloimmunity in solid organ transplant recipients. We have developed an immune-focused IMC panel, clustering algorithm, and analysis

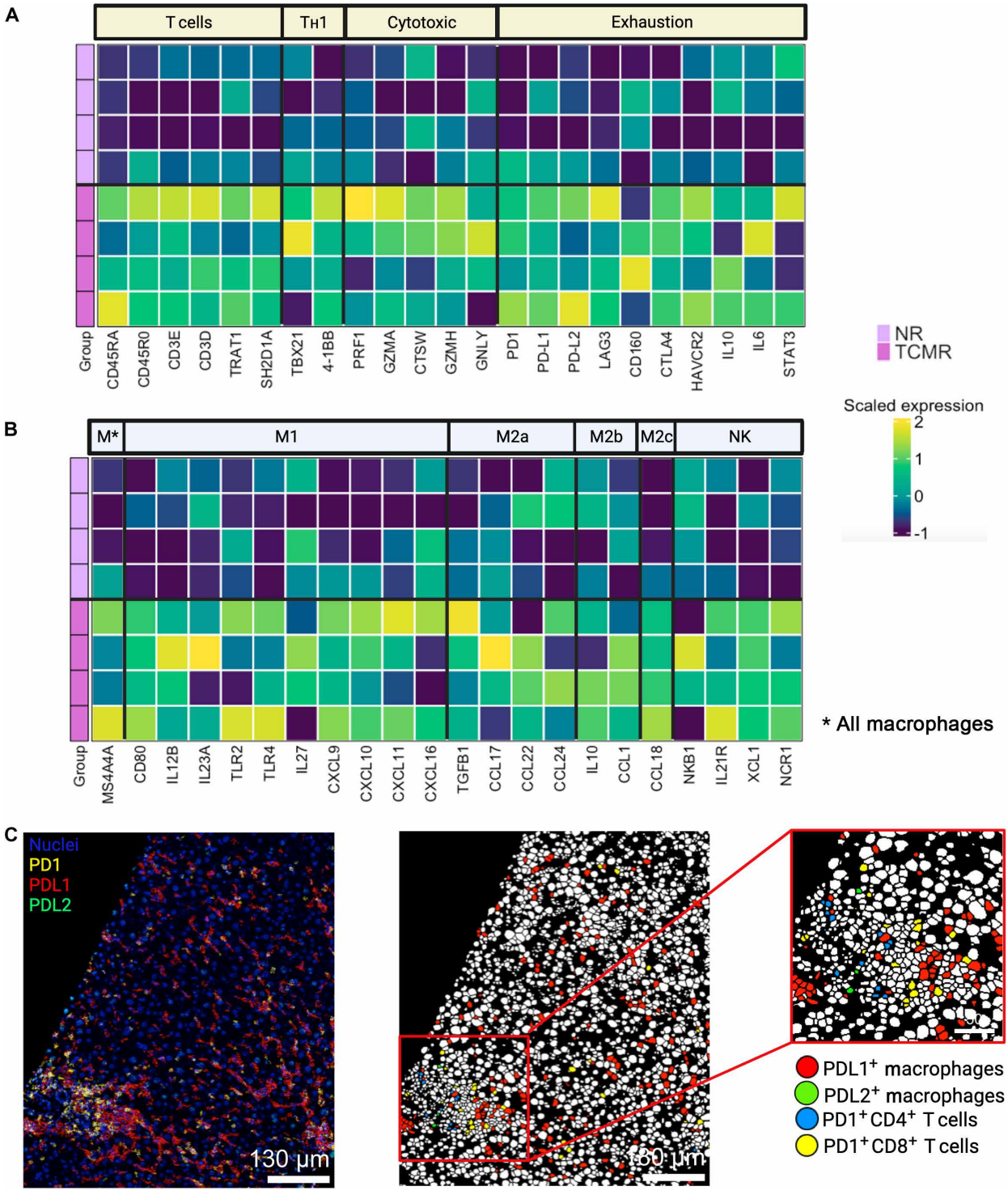

Fig. 7. In depth molecular characterization of tissue using bulk RNA-seq confirms the exhaustion signature associated with active TCMR. (**A**) Sequential FFPE tissue sections obtained from a subgroup of most representative four NR and four TCMR FFPE of cellular compositions observed for each clinical group using IMC were analyzed using nCounter bulk RNA-seq. The heatmap visualizes the scaled expression of genes corresponding to generic T cells, T helper 1 (T_H1), cytotoxic, and exhausted phenotypes in both NR and TCMR. Activated, cytotoxic, and exhausted T cell genes showed a greater expression in active TCMR when compared to NR. (**B**) Heatmap of scaled expression values of macrophage and NK-related genes including M1, M2a, M2b, and M2c phenotypes along with NK-associated genes. Genes belonging to both M1 and M2 polarized macrophages showed a greater expression in active TCMR than NR; similarly, NK-associated gene expression was higher in TCMR. (**C**) To confirm bulk RNA-seq data, TCMR sections were examined for PD1, PDL1, and PDL2 (left) protein expression using IMC. The middle and zoomed in panel on the right show cell mask outlines colored blue for $PD1^+CD4^+$ T cells, yellow for $PD1^+CD8^+$ T cells, red for $PDL1^+CD68^+$ macrophages, and green for $PDL2^+CD68^+$ macrophages. This visually confirms the presence of exhausted phenotype T cells and their interaction with macrophages expressing PDL1 and PDL2 ligands in active TCMR.

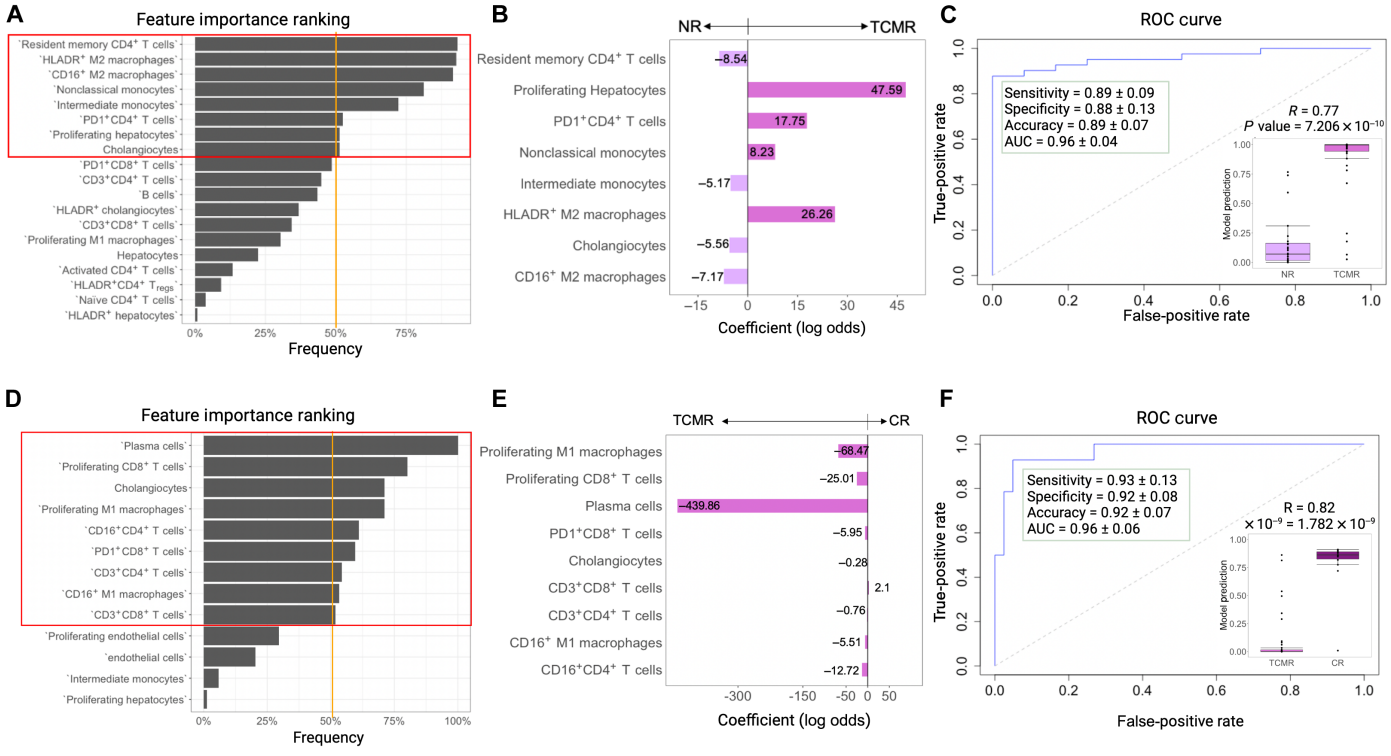

Fig. 8. Identification of cellular features in liver allograft biopsies that are highly predictive for discriminating active TCMR from NR and CR. (**A**) Bootstrapping using LASSO regression identified the top highly ranked features which are predictive of NR versus TCMR. (**B**) On the basis of the model, identified cell subpopulations well suited for distinguishing TCMR from NR include proliferating hepatocytes, $PD1^+CD4^+$ T cells, nonclassical monocytes, and $HLADR^+$ M2 macrophages. Positive coefficient indicates that an increase of that cell subpopulation increases the likelihood of TCMR, while negative coefficient indicates that an increase of that cell subpopulation decreases the likelihood of TCMR, thus increasing the likelihood of NR. (**C**) Evaluation metrics for predictive model built using highly ranked cell subpopulations identified in A. The model shows a sensitivity of 0.89 ± 0.09, specificity of 0.88 ± 0.13, accuracy of 0.89 ± 0.07, and AUC of 0.96 ± 0.04 (means ± SD). Spearman correlation coefficient between median predicted and actual outcomes $R = 0.77$; P value $= 7.206 \times 10^{-10}$ (Wilcoxon rank-sum test). (**D**) Bootstrapping using LASSO regression model identified the top highly ranked features, which are predictive of TCMR versus CR. (**E**) On the basis of the model, identified subpopulations well suited for distinguishing TCMR from CR include proliferating M1 macrophages, proliferating $CD8^+$ T cells, plasma cells, $PD1^+CD8^+$ T cells, cholangiocytes, $CD3^+CD4^+$ T cells, $CD16^+$ M1 macrophages, and $CD16^+CD4^+$ T cells. Positive coefficient indicates that an increase of that cell subpopulation increases the likelihood of CR, while negative coefficient indicates that an increase of that cell subpopulation decreases the likelihood of CR, thus increasing the likelihood of TCMR. (**F**) Evaluation metrics for predictive model built using highly ranked cell subpopulations identified in (D). The model shows a sensitivity of 0.93 ± 0.13, specificity of 0.92 ± 0.08, accuracy of 0.92 ± 0.07, and AUC of 0.96 ± 0.06 (means ± SD). Spearman correlation coefficient between median predicted and actual outcomes $R = 0.82$; P value $= 1.7827 \times 10^{-9}$ (Wilcoxon rank-sum test). ROC, receiver operating characteristic.

pipeline that enables high-resolution, highly multiplexed analysis in the immune microenvironment in human tissue. Unlike the cancer tumor microenvironment, which has remarkable phenotypic variability between patients and even within the same specimen, our analysis confirms central tenants of transplant immunology, namely, that the pathologic features within the AME are similar across individuals despite differences in patient demographics, underlying etiology of liver disease, features of the donor organ, and timing of rejection episodes. Thus, study of the AME offers an ideal application and proof of concept for further development of spatial proteomics immunologic analyses using archival biopsy specimens, particularly with expansion of T cell and macrophage/monocyte lineage markers as they become available. Exploration of discrete immune subpopulations within the AME of core needle liver biopsies has identified specific immune subsets of T lymphocytes expressing PD1 molecules that are enriched in active TCMR and largely absent in CR, with confirmation using RNA-seq, providing insights into the underpinnings and evolution of liver allograft rejection. Last, these data were harnessed to create a predictive model of TCMR and CR using a subset of cell types, which offers new targets for biomarker development and therapeutic targets in patients with active TCMR. Specifically, our data suggest that deeper investigation of exhaustion markers in the blood could offer diagnostic value both for identification of subclinical TCMR episodes and tracking resolution following treatment. Furthermore, our data support the exploration of targeted immunotherapies designed to promote immune exhaustion as therapeutic strategies to treat post-transplant rejection episodes in clinical LT.

Single-cell analysis of the AME has uncovered substantial complexity in allograft rejection, involving at least 32 distinct immune subpopulations. Nearly all prior studies of LT rejection have focused on one or few immune cell types (*47*, *48*). In active TCMR, our data demonstrate that diverse cell populations contribute to the underlying pathophysiology. It is increasingly recognized that spatial context is important to completely describe disease phenotypes and that these multiplexed spatial techniques will have important clinical implications (*49*). A recent study in clinical LT examined immune cell type pairs at high

resolution to evaluate immune synapse formation and used these data to predict likelihood of immunosuppression weaning success (*11*). Visual assessment of TCMR tissue suggest that immune cells might be grouped into inflammatory tertiary lymphoid organs (iTLOs) (Figs. 2A, 3A, and 4A, and figs. S5A and S6A). iTLOs have been described in allograft rejection after solid organ transplantation (*50*–*52*). In humans, iTLOs composed of a variable proportion of T and B cells, macrophages, and high endothelial venules have been characterized during recurrent acute rejection in both cardiac and renal allografts (*53*–*55*). Also, we observed a similar small but higher proportion of B cells in the TCMR group when compared to NR or CR (Fig. 1E). Our antibody panel does not currently include markers that would allow the identification of regulatory B cells such as CD24 or IL-10. We will consider adding these markers in our next panel, recognizing that this is a very rare population overall but potentially interesting to further clarify the alloimmune response in LT. These data, together with our results, suggest that further characterization of important features of the AME will provide valuable insights into predicting clinical outcomes, including response to treatment, with greater precision than is currently possible.

Arising from the complex microenvironment was a central theme of PD1 pathway involvement and a cellular milieu with features of immune exhaustion during active TCMR episodes post-LT. Our study design captures clinical specimens before initiation of treatment, the mainstay of which are CNIs, which are designed to indiscriminately prevent T cell proliferation and come with potentially severe side effects. Fortunately, the immune system has physiologic mechanisms to dampen this immune response through PD-L1, a molecule that when knocked out in mice results in auto-immunity, and is also important in chronic inflammatory states (*15*, *56*, *57*). Our results show $PD1^+CD4^+$ T cells and $PD1^+CD8^+$ T cells are expanded in TCMR and spatially interacting with other $CD4^+$ and $CD8^+$ subpopulations, as well as $HLADR^+$ M2 macrophages. We also show that PD1+ T cells and macrophages expressing both PD1 ligands were present in TCMR. Predictive modeling classified $PD1^+CD4^+$ T cells as a feature distinguishing TCMR from NR, while $PD1^+CD8^+$ T cells were identified as a feature distinguishing TCMR from CR. Together, these data indicate that immune exhaustion may be a key process in active TCMR in clinical LT and suggest further investigation of the PD1 pathway to elucidate its role in the pathophysiology of TCMR.

Dysregulated exhaustion states are increasingly recognized as pathways that cancer cells manipulate to mediate immune escape, leading to development of immune checkpoint inhibitor therapies to enhance antitumor adaptive immune responses. Our data suggest the opposite therapeutic approach could be explored to counteract pro-inflammatory responses during acute TCMR via augmentation of physiologic exhaustion. Prior work using PD-1 agonists in other pro-inflammatory states, including neutrophilic asthma, has demonstrated that therapies designed to promote T cell exhaustion can mitigate inflammation, suggesting that application of these drugs that are already in clinical development to clinical LT rejection may offer a treatment paradigm for this common post-transplant entity in the modern era (*16*). Given that infection continues to be a leading cause of mortality in the LT population, development of more focused immunotherapies has the potential to offer a lower risk option when compared to corticosteroids or anti-thymocyte globulin, which require escalation of infection prophylaxis.

Presently, and for the past 60 years, pathologic detection of allograft rejection has been conducted using hematoxylin and eosin staining. The Banff RAI is then used to characterize rejection by evaluation of portal and/or perivenular inflammatory (immune) infiltrates (*58*). Our study suggests that spatial relationships between immune cells and cholangiocytes or endothelial cells may be less important mechanistically, which is something to consider as the Banff criteria for TCMR in LT are re-evaluated in the future (Fig. 5E and fig. S7, E and F). Rather, investigation into the presence or absence of certain immune subpopulations may better inform important considerations of TCMR such as steroid-resistant disease, a disease that often progresses to CR and drives late graft failure. Future studies using IMC to study the AME through TCMR and following treatment to detect features associated with response and treatment resistance, combined with predictive modeling, may bring value in this regard. A recent study used IMC combined with deep learning to predict lung adenocarcinoma progression and patient survival after surgery with high accuracy (*59*). Harnessing multiplexed data together with emerging artificial intelligence tools such as deep learning may have profound diagnostic and prognostic value, both in clinical practice and in monitoring responses to treatment in clinical trials. A major benefit of IMC is its application to archival FFPE samples from a small core biopsy, which represents the most easily accessible and available specimen in clinical settings. In addition, compared to current spatial transcriptomic and bulk RNA-seq platforms, IMC provides true single-cell resolution of the examined tissue while capturing rare cell types. Furthermore, proteomics-based platforms such as IMC more accurately reflect single-cell phenotypes, given that RNA is not always linearly correlated with protein translation (*60*). A strength of our study involves examination of clinically diagnostic periportal areas selected by a specialist pathologist, resulting in more than 5000 cells per ROI. This is comparable to cell counts obtained from single-cell RNA-seq experiments in human liver, but our data represent the most clinically relevant diagnostic area with spatial coordinates, rather than a random set of 5000 cells obtained from tissue that might be subject to potential bias caused by tissue dissociation and processing techniques necessary to create a single-cell suspension (*61*). It would be ideal to perform complementary functional assays on immune cells isolated from fresh liver biopsy tissue. Unfortunately, it is impossible to capture enough rare populations from a fresh biopsy with current technologies. In future work, we plan to expand our IMC panel with activation/exhaustion markers as they become available to understand the phenotype of these rare populations in more detail. Ultimately, it is possible that highly multiplexed immunohistochemistry such as IMC could be applied to identify individual patients who may benefit from more focused therapeutic regimens to achieve more personalized management.

Our analysis is limited by being unable to conduct complementary single-cell transcriptomics or cell culture–based assays as our study was performed on a retrospective set of tissue FFPE specimens collected during routine clinical care. Furthermore, there is the possibility of cell classification errors within our IMC dataset, particularly within the hepatocyte metacluster that was classified based on exclusion of other cell types. To minimize this risk, we conducted an extensive review of all annotated tissue specimens alongside raw marker expressions to ensure that tissue labeling was optimized. T_{reg} populations were classified using established markers ($CD3^+CD4^+FoxP3^+$ T cells), but we acknowledge that these markers may not fully capture all human T_{reg} and will continue to refine our panel with additional markers including CD25 and CD127, which will improve the characterization of this cell phenotype (*31*). Because of the unexpected importance

of PD1$^+$ T cell phenotypes in our results, our IMC dataset lacked additional exhaustion markers, which will be incorporated for future studies. Also, IMC is expensive when compared to traditional immunohistochemistry and requires antibody validation and accurate titration to provide biologically meaningful results. However, when compared to more costly spatial transcriptomics platforms (e.g., Visium or GeoMX), none offer the same capacity for single-cell resolution in archival FFPE core needle biopsies. We also acknowledge that combination of protein and RNA probes can provide more information on cellular states (*62*). Our patient sample size was somewhat limiting for our results, particularly with predictive modeling in CR; however, our analyses support our study being adequately powered for the evaluation of important cell subpopulations and in the modeling of active TCMR. Last, mixed pathologies could make biopsy interpretation difficult and acknowledge that prospective validation with a larger dataset is the next step. We are encouraged by data from the INTERLIVER clinical rejection assays that are based on microarray data from a smaller cohort of TCMR than ours and do not differentiate immunosuppression regimen or underlying diagnosis (*10*). In that study, they were able to differentiate "acute dysfunction–NR" from TCMR. Because our approach has true single-cell resolution with the addition of a spatial data layer, it is possible that IMC may offer a more precise approach to differentiate mixed pathology in future studies.

Here, we provide a detailed and spatially resolved atlas of clinical liver allograft rejection. Highly multiplexed IMC-based analyses uncovered unique features of the AME and predictive features of rejection states. We further identified a cellular milieu with unique features of immune exhaustion in active TCMR, suggesting the PD-1 pathway as a potentially therapeutic target in liver allograft rejection. This work provides a conceptual framework for investigation of inflammatory processes in immunologically complex histological diseases of the liver using clinical samples.

MATERIALS AND METHODS

This study was approved by the Health Science Campus Institutional Review board of the University of Southern California (HS-18-00708) and, due to the retrospective nature of this study, was considered exempt from requiring consent for research analysis of archival specimens.

Patients

LT recipients were retrospectively identified using our institutional transplant database. Patients >18 years at the time of transplant who underwent biopsy of their liver allograft to rule out suspected TCMR or patients with CR undergoing retransplantation between January 2000 and December 2021 met inclusion criteria. Patients were excluded if the histologic diagnosis was associated with reactivation or concurrent viral infection (i.e., hepatitis C or cytomegalovirus), anatomic causes of graft dysfunction (i.e., vascular stenoses and/or biliary strictures), or advanced fibrosis (bridging fibrosis based on Trichrome staining). All biopsies were performed before initiation of treatment of rejection. Cases were reviewed by a pathologist with expertise in LT to prioritize selection of patients with RAI ≥ 4 for the TCMR group [$n = 41$ patients, 58 ROIs, median RAI of 5, and interquartile range (IQR) of 5 to 6)]. LT recipients who did not have evidence of rejection on their biopsy (RAI = 0) were selected for the NR group ($n = 24$). The CR patients ($n = 14$) were identified at the time of retransplant for CR with histologic confirmation of CR in the explant.

Clinical data and demographics

Demographics and clinical parameters were obtained via comprehensive chart review and included age, sex, ethnicity, race, age at transplant, serum biochemistries, immunosuppression regimens, and all biopsy data including indication for biopsy, timing of biopsy in relation to LT, and pathology reports. Relevant demographic variables are summarized for the cohort in table S2. For consistency, RAI score and detailed breakdown of subscores were independently performed by a liver-specialized pathologist. This review showed close agreement with the pathologic evaluation performed at the time of biopsy.

Imaging mass cytometry

Sections from FFPE tissue blocks obtained and stored at room temperature as part of clinical standard of care during liver biopsy or transplant (4 μm) were selected by the pathologist to identify 1 mm^2 ROIs for IMC acquisition focusing on periportal regions of the biopsies most representative of what was examined for clinical assessment of RAI. The SC2 Core Facility at Children's Hospital–Los Angeles performed all staining and image acquisition for this study. Slides were stained using a custom 22-marker antibody panel. Structural markers included two nuclear intercalator dyes, collagen, CD31 (vascular endothelium), and CK7 (bile ducts). Immune lineage markers included CD3, CD4, CD8, CD20, CD68, and CD11b, and functional or phenotypic markers included CD279 (PD1), FoxP3, Ki67, and Granzyme B among others (table S3). IMC staining was performed using techniques described previously (*37*). Ninety-six ROIs (average of 1.2 ROI per patient) were ablated using the Hyperion Imaging System (Standard Biotools) at a power range of 3.5 to 4.5 with a laser frequency at 200 Hz. Data were supplied as .txt and .mcd files for use in segmentation and downstream analyses.

Image preprocessing and segmentation

Preprocessing steps were completed using the MATLAB package MAUI (MBI Analysis User Interface) (*63*). CD68 was used as the basis for channel spillover correction, and noise removal and channel aggregate removal steps were implemented individually on each channel. Pre-processing was conducted in three batches by clinical outcome (NR, TCMR, and CR) to account for staining background and noise differences between disease states. Cell segmentation was performed using Mesmer (DeepCell) and following the Bodenmiller Steinbock pipeline (*45*). Image preprocessing was performed in MATLAB (version R2022b) and Python (version 3.10.8).

Single-cell phenotyping

Cell segmentation outputs were loaded into R (version 4.2.2) to perform downstream analysis. Patient ID and clinical group identifiers were added to the single-cell experiment object (*64*). Data were arcsin-transformed using a cofactor of 5 and standardized by channel to account for differences in signal intensities.

Metaclusters were identified using a supervised clustering approach outlined in table S4. Labeling accuracy was verified by reviewing concurrent metacluster label and channel expression on tissue sections. Masks were used to visualize cell labels ("cytomapper::plotCells") (*65*). TIFF images were scaled, and channel signals were normalized and visualized individually ("cytomapper::plotPixels"). For each patient, metacluster proportions were calculated using the overall cell count as baseline and statistically compared across clinical groups. Subclustering was performed on the five most relevant immune metaclusters (CD4$^+$ T cells, CD8$^+$ T cells, B cells, macrophages, and monocytes)

using a semi-supervised approach. A total of 30 subclusters were identified, leading to a final 32 immune clusters and 9 non-immune clusters in the overall dataset. Dimensionality reduction was performed using t-SNE to visualize meta- and subclusters by clinical outcome (*66*). A t-SNE was also used to visualize possible batch effects between patients. Batch correction was performed using the mutual nearest neighbor method, but ultimately not used for downstream analysis to avoid possibly also eliminating biological differences present in the data (*67*).

Trajectory inference

To investigate whether cell phenotypes identified via IMC represented a pseudotemporal evolution of the AME in LT rejection, we performed trajectory inference on each metacluster, which has been used by other groups working with mass cytometry data (*33*–*35*). Trajectories were identified by Slingshot, an algorithm that can model branching lineages in single-cell data, based on metacluster-specific dimensionality reduction using uniform manifold approximation and projection (*32*, *68*). To ensure proper orientation of each trajectory, a coarse clustering was performed using *k*-means ($k = 2$, except for $CD8^+$ T cells, where $k = 5$) and the cluster with the highest proportion of cells from NR samples was set as the initial cluster.

Spatial analysis

The k-nearest neighbor approach ($k = 10$) was used to create the cell-cell interaction graph, which was visualized on tissue using the "imcRtools::plotSpatial" function (*45*). Neighborhood analysis ("imcRtools::testInteractions") was implemented on each clinical subset to analyze pairwise interactions between metaclusters and between subclusters and to compare differences across clinical outcomes (*45*). Cell-cell interactions were calculated using permutation testing (1000 permutations, $\alpha = 0.01$) to determine whether cell types interact more (attraction) or less (avoidance) frequently than random permutations. Graph network analysis using igraph was used to visualize subcluster interactions (*69*).

CN analysis was implemented ("imcRtools::aggregateNeighbors") using the constructed k-nearest neighbor spatial graph ($k = 10$). Cells were reclustered on the basis of the cell types in their direct spatial neighborhood to obtain nine CNs. Cell-type abundance of each CN was visualized on a heatmap to aid CN annotation. For each patient, CN proportions were calculated, visualized, and statistically tested to detect any differences across clinical group. CNs were also visualized on the tissue to detect any visual differences in spatial composition across clinical group.

Because of the spatial relevance of TCMR infiltrates to the vascular endothelium (based off clinical Banff criteria RAI scoring), the median distance of each cell type (meta- and subclusters) to endothelial cells was calculated and compared across clinical groups.

Predictive modeling

LASSO regression was used to build predictive models of NR versus TCMR, TCMR versus CR, and NR versus CR. LASSO is a shrinkage method that aids in feature selection and avoids overfitting. LASSO adds an L1 regularization term (sum of absolute values of the coefficients) so that the selected coefficients minimize the loss function $L(\beta) = ||\mathbf{Y} - \mathbf{X}\beta||^2 + \lambda_1||\beta||_1$, where $\mathbf{Y}$ is the vector of the binary clinical outcome, $\mathbf{X}$ is the feature matrix, β is the vector of coefficients, and $\lambda_1$is the regularization coefficient. A fivefold CV technique was used to find the optimal λ_1 value. For each comparison, model building was done using those cell types found to be statistically significant in the pairwise comparisons as input. Bootstrapping, a sampling with replacement technique, was implemented to rank the importance of all features (5000 iterations). In each iteration, logistic LASSO regression was implemented on a subset of the data and nonzero coefficients were stored. Variable frequency was determined, and variables with ≥50% frequency were selected for the final model. To evaluate model performance, and because we did not have access to an external dataset for validation, data were cross-validated by repeatedly randomly splitting into training and validation sets at a 75:25 ratio (1000 iterations). This ensures the model is evaluated on observations not used during training. In each iteration, the model was trained on the training set using the features identified during bootstrapping. Clinical outcome was then predicted on the validation set and stored alongside performance metrics (sensitivity, specificity, accuracy, and AUC). Final model coefficients were obtained by averaging all coefficients. Final model performance was calculated using the evaluation metrics obtained from all iterations (means ± SD). Receiver operating characteristic (ROC) curve was calculated using the median prediction of each patient. Correlation between the median prediction and actual clinical outcome was calculated using Spearman correlation, and significance was tested using the Wilcoxon rank-sum test.

nCounter transcriptomic analysis

A subset of representative tissue sections from the IMC analysis based on cellular composition was selected (four NR and four TCMR), and at least five sequential 5-mm FFPE sections per block were combined for RNA extraction using the RNeasy Kit (QIAGEN). Extracted RNA was quantified using the NanoDrop system (Thermo Fisher Scientific), and 200 ng of total RNA was used for gene expression analysis. Samples were processed using the nCounter Nanostring platform and the PanCancer Immune Profiling and T cell repertoire panels according to the manufacturer's guidelines (NanoString Technologies). Raw counts were normalized using internal positive standards and housekeeping genes with the nSolver Analysis 4.0 and Advanced Analysis 2.0 software (NanoString Technologies). Expression of scaled $\log_2$ gene counts were visualized using heatmaps to determine expression differences between NR and TCMR samples. Publicly available data from a study of six patients who underwent IL-2 therapy and subsequently had rejection episodes within 6 months after treatment was used for external validation (*31*). The fold change in mean gene expression between NR and TCMR as well as baseline and 4 weeks after treatment was compared to show similarity in gene up-regulation.

Statistical analysis

The Shapiro-Wilk test was used to test for normality. One-way analysis of variance (ANOVA) and two-sample *t* test were used to analyze parametric data. Kruskal-Wallis and two-sample Wilcoxon rank-sum tests were used to analyze nonparametric data. All tests were performed as two-sided. *P* values were corrected for multiple testing using the Holm method. Number of cells for each meta- and subcluster were reported as median [IQR]. A 0.05 *P* value cutoff was used throughout the analysis to determine statistical significance. Boxplots, used to visualize proportions, show median (center line) and lower and upper quartiles (box limits). Boxplot whiskers represent the minimum and maximum values—calculated as 1.5 × IQR (interquartile range) away from the box limits—and individual dots represent outliers. Seeds were set to allow for reproducibility. All statistical tests were carried out in R (version 4.2.2).

Supplementary Materials

This PDF file includes:

Figs. S1 to S9

Tables S1 to S4

REFERENCES AND NOTES

1. A. Shaked, R. M. Ghobrial, R. M. Merion, T. H. Shearon, J. C. Emond, J. H. Fair, R. A. Fisher, L. M. Kulik, T. L. Pruett, N. A. Terrault, A2ALL Study Group, Incidence and severity of acute cellular rejection in recipients undergoing adult living donor or deceased donor liver transplantation. *Am. J. Transplant.* **9**, 301–308 (2009).
2. A. S. Bartlett, R. Ramadas, S. Furness, E. Gane, J. L. McCall, The natural history of acute histologic rejection without biochemical graft dysfunction in orthotopic liver transplantation: A systematic review. *Liver Transpl.* **8**, 1147–1153 (2002).
3. J. Levitsky, D. Goldberg, A. R. Smith, S. A. Mansfield, B. W. Gillespie, R. M. Merion, A. S. F. Lok, G. Levy, L. Kulik, M. Abecassis, A. Shaked, Acute rejection increases risk of graft failure and death in recent liver transplant recipients. *Clin. Gastroenterol. Hepatol.* **15**, 584–593.e2 (2017).
4. E. M. Haddad, V. C. McAlister, E. Renouf, R. Malthaner, M. S. Kjaer, L. L. Gluud, Cyclosporin versus tacrolimus for liver transplanted patients. *Cochrane Database Syst. Rev.* **2006**, CD005161 (2006).
5. A. J. Demetris, K. P. Batts, A. P. Dhillon, L. Ferrell, J. Fung, S. A. Geller, J. Hart, P. Hayry, W. J. Hofmann, S. Hubscher, J. Kemnitz, G. Koukoulis, R. G. Lee, K. J. Lewin, J. Ludwig, R. S. Markin, L. M. Petrovic, M. J. Phillips, B. Portmann, J. Rakela, P. Randhawa, F. P. Reinholt, M. Reyne's, R. Reyne's, M. Robert, H. Schlitt, K. Solez, D. Snover, E. Taskinen, S. N. Thung, G. W. Tillery, R. H. Wiesner, D. G. D. Wight, J. W. Williams, H. Yamabe, Banff Schema for grading liver allograft rejection: An international consensus document. *Hepatology* **23**, 658–663 (1997).
6. A. J. Demetris, C. Bellamy, S. G. Hübscher, J. O'Leary, P. S. Randhawa, S. Feng, D. Neil, R. B. Colvin, G. M. Caughan, J. J. Fung, A. Del Bello, F. P. Reinholt, H. Haga, O. Adeyi, A. J. Czaja, T. Schiano, M. I. Fiel, M. L. Smith, M. Sebagh, R. Y. Tanigawa, F. Yilmaz, G. Alexander, L. Baiocchi, M. Balasubramanian, I. Batal, A. K. Bhan, J. Bucuvalas, C. T. S. Cerski, F. Charlotte, M. E. de Vera, M. El Monayeri, P. Fontes, E. E. Furth, A. S. H. Gouw, S. Hafezi-Bakhtiari, J. Hart, E. Honsova, W. Ismail, T. Itoh, N. C. Jhala, U. Khettry, G. B. Klintmalm, S. Knechtle, T. Koshiba, T. Kozlowski, C. R. Lassman, J. Lerut, J. Levitsky, L. Licini, R. Liotta, G. Mazariegos, M. I. Minervini, J. Misdraji, T. Mohanakumar, J. Mölne, I. Nasser, J. Neuberger, M. O'Neil, O. Pappo, L. Petrovic, P. Ruiz, Ö. Sağol, A. S. Fueyo, E. Sasatomi, A. Shaked, M. Shiller, T. Shimizu, B. Sis, A. Sonzogni, H. L. Stevenson, S. N. Thung, G. Tisone, A. C. Tsamandas, A. Wernerson, T. Wu, A. Zeevi, Y. Zen, *Am. J. Transplant.* **16**, 2816–2835 (2016).
7. D. Thangarajah, M. O'Meara, A. Dhawan, Management of acute rejection in paediatric liver transplantation. *Pediatric Drugs* **15**, 459–471 (2013).
8. V. Ronca, G. Wootton, C. Milani, O. Cain, The immunological basis of liver allograft rejection. *Front. Immunol.* **11**, 2155 (2020).
9. A. Sánchez-Fueyo, T. B. Strom, Immunologic basis of graft rejection and tolerance following transplantation of liver or other solid organs. *Gastroenterology* **140**, 51–64 (2011).
10. K. Madill-Thomsen, M. Abouljoud, C. Bhati, M. Ciszek, M. Durlik, S. Feng, B. Foroncewicz, I. Francis, M. Grąt, K. Jurczyk, G. Klintmalm, M. Krasnodębski, G. McCaughan, R. Miquel, A. Montano-Loza, D. Moonka, K. Mucha, M. Myślak, L. Pączek, A. Perkowska-Ptasińska, G. Piecha, T. Reichman, A. Sanchez-Fueyo, O. Tronina, M. Wawrzynowicz-Syczewska, A. Więcek, K. Zieniewicz, P. F. Halloran, The molecular diagnosis of rejection in liver transplant biopsies: First results of the INTERLIVER study. *Am. J. Transplant.* **20**, 2156–2172 (2020).
11. M. A. Wood-Trageser, D. Lesniak, A. Gambella, K. Golnoski, S. Feng, J. Bucuvalas, A. Sanchez-Fueyo, A. J. Demetris, Next-generation pathology detection of T cell–antigen-presenting cell immune synapses in human liver allografts. *Hepatology* **77**, 355–366 (2023).
12. J. Yu, Z. Liu, C. Li, Q. Wei, S. Zheng, K. Saeb-Parsy, X. Xu, Regulatory t cell therapy following liver transplantation. *Liver Transpl.* **27**, 264–280 (2021).
13. G. P. Whitehouse, A. Hope, A. Sanchez-Fueyo, Regulatory T-cell therapy in liver transplantation. *Transpl. Int.* **30**, 776–784 (2017).
14. L. V. Riella, A. M. Paterson, A. H. Sharpe, A. Chandraker, Role of the PD-1 Pathway in the Immune Response. *Am. J. Transplant.* **12**, 2575–2587 (2012).
15. A. H. Sharpe, K. E. Pauken, The diverse functions of the PD1 inhibitory pathway. *Nat. Rev. Immunol.* **18**, 153–167 (2018).
16. D. G. Helou, C. Quach, M. Fung, J. D. Painter, B. P. Hurrell, Y. H. Eddie Loh, E. Howard, P. Shafiei-Jahani, P. Soroosh, A. H. Sharpe, O. Akbari, Human PD-1 agonist treatment alleviates neutrophilic asthma by reprogramming T cells. *J. Allergy Clin. Immunol.* **151**, 526–538.e8 (2023).
17. R. Pike, N. Thomas, S. Workman, L. Ambrose, D. Guzman, S. Sivakumaran, M. Johnson, D. Thorburn, M. Harber, B. Chain, H. J. Stauss, PD1-expressing T cell subsets modify the rejection risk in renal transplant patients. *Front. Immunol.* **7**, 126 (2016).
18. E. Ozkaynak, L. Wang, A. Goodearl, K. M. Donald, S. Qin, T. O'Keefe, T. Duong, T. Smith, J.-C. Gutierrez-Ramos, J. B. Rottman, A. J. Coyle, W. W. Hancock, Programmed death-1 targeting can promote allograft survival. *J. Immunol.* **169**, 6546–6553 (2002).
19. M. Bishawi, D. Bowles, M. M. Pla, F. Oakes, Y. Chiang, J. Schroder, C. Milano, C. Glass, PD-1 and PD-L1 expression in cardiac transplantation. *Cardiovasc. Pathol.* **54**, 107331 (2021).
20. M. Takatsuki, S. Uemoto, Y. Inomata, H. Egawa, T. Kiuchi, S. Fujita, M. Hayashi, T. Kanematsu, K. Tanaka, Weaning of immunosuppression in living donor liver transplant recipients. *Transplantation* **72**, 449–454 (2001).
21. A. Choudhary, D. M. Brinkley, S. Besharati, W. C. Meijers, J. B. Atkinson, K. Amancherla, Q. Zhu, S. Huang, L. S. Nguyen, J.-E. Salem, E. Ammirati, J. A. Lindenfeld, R. A. Anders, J. Moslehi, Circulation: Heart failure PD-L1 (Programmed Death Ligand 1) as a marker of acute cellular rejection after heart transplantation. *Circ. Heart Fail.* **14**, e008563 (2021).
22. K. Tanaka, M. J. Albin, X. Yuan, K. Yamaura, A. Habicht, T. Murayama, M. Grimm, A. M. Waaga, T. Ueno, R. F. Padera, H. Yagita, M. Azuma, T. Shin, B. R. Blazar, D. M. Rothstein, M. H. Sayegh, N. Najafian, PDL1 is required for peripheral transplantation tolerance and protection from chronic allograft rejection. *J. Immunol.* **179**, 5204–5210 (2007).
23. X.-L. Shi, S. Mancham, B. E. Hansen, R. J. De Knegt, J. De Jonge, L. J. W. Van Der Laan, F. Rivadeneira, H. J. Metselaar, J. Kwekkeboom, Counter-regulation of rejection activity against human liver grafts by donor PD-L1 and recipient PD-1 interaction. *J. Hepatol.* **64**, 1274–1282 (2016).
24. G. Syal, M. Fausther, J. A. Dranoff, Advances in cholangiocyte immunobiology. *Am. J. Physiol. Gastrointest. Liver Physiol.* **303**, G1077–G1086 (2012).
25. S. M. Cruickshank, J. Southgate, P. J. Selby, L. K. Trejdosiewicz, Expression and cytokine regulation of immune recognition elements by normal human biliary epithelial and established liver cell lines in vitro. *J. Hepatol.* **29**, 550–558 (1998).
26. L. Campana, H. Esser, M. Huch, S. Forbes, Liver regeneration and inflammation: from fundamental science to clinical applications. *Nat. Rev. Mol. Cell Biol.* **22**, 608–624 (2021).
27. Y. Wen, J. Lambrecht, C. Ju, F. Tacke, Hepatic macrophages in liver homeostasis and diseases-diversity, plasticity and therapeutic opportunities. *Cell. Mol. Immunol.* **18**, 45–56 (2020).
28. A. Barbetta, B. Rocque, D. Sarode, J. A. Bartlett, J. Emamaullee, Revisiting transplant immunology through the lens of single-cell technologies. *Semin. Immunopathol.* **45**, 91–109 (2022).
29. F. Z. El Hentati, F. Gruy, C. Iobagiu, C. Lambert, Variability of CD3 membrane expression and T cell activation capacity. *Cytometry B Clin. Cytom.* **78**, 105–114 (2010).
30. L. Nicolas, G. Monneret, A. L. Debard, A. Blesius, M. C. Gutowski, G. Salles, J. Bienvenu, Human gammadelta T cells express a higher TCR/CD3 complex density than alphabeta T cells. *Clin. Immunol.* **98**, 358–363 (2001).
31. T. Y. Lim, E. Perpiñán, M. C. Londoño, R. Miquel, P. Ruiz, A. S. Kurt, E. Kodela, A. R. Cross, C. Berlin, J. Hester, F. Issa, A. Douiri, F. H. Volmer, R. Taubert, E. Williams, A. J. Demetris, A. Lesniak, G. Bensimon, J. J. Lozano, M. Martinez-Llordella, T. Tree, A. Sánchez-Fueyo, Low dose interleukin-2 selectively expands circulating regulatory T cells but fails to promote liver allograft tolerance in humans. *J. Hepatol.* **78**, 153–164 (2023).
32. K. Street, D. Risso, R. B. Fletcher, D. Das, J. Ngai, N. Yosef, E. Purdom, S. Dudoit, Slingshot: Cell lineage and pseudotime inference for single-cell transcriptomics. *BMC Genomics* **19**, 477 (2018).
33. N. Damond, S. Engler, V. R. T. Zanotelli, P. L. Herrera, M. A. Atkinson, B. B. Correspondence, A map of human type 1 diabetes progression by imaging mass cytometry. *Cell Metab.* **29**, 755–768.e5 (2019).
34. Y. Dai, A. Xu, J. Li, L. Wu, S. Yu, J. Chen, W. Zhao, X. J. Sun, J. Huang, CytoTree: an R/Bioconductor package for analysis and visualization of flow and mass cytometry data. *BMC Bioinformatics* **22**, 138 (2021).
35. S. V. Stassen, G. G. K. Yip, K. K. Y. Wong, J. W. K. Ho, K. K. Tsia, Generalized and scalable trajectory inference in single-cell omics data with VIA. *Nat. Commun.* **12**, 5528 (2021).
36. W. W. Hancock, N. M. Thomson, R. C. Atkins, Composition of interstitial cellular infiltrate identified by monoclonal antibodies in renal biopsies of rejecting human renal allografts. *Transplantation* **35**, 458–462 (1983).
37. N. Ung, C. Goldbeck, C. Man, J. Hoeflich, R. Sun, A. Barbetta, N. Matasci, J. Katz, J. S.-H. Lee, S. Chopra, S. Asgharzadeh, M. Warren, L. Sher, R. Kohli, O. Akbari, Y. Genyk, J. Emamaullee, Adaptation of imaging mass cytometry to explore the single cell alloimmune landscape of liver transplant rejection. *Front. Immunol.* **13**, 831103 (2022).
38. F. Ordikhani, V. Pothula, R. Sanchez-Tarjuelo, S. Jordan, Macrophages in Organ Transplantation. *Front. Immunol.* **11**, 582939 (2020).
39. K. Lackner, S. Ebner, K. Watschinger, M. Maglione, Multiple shades of Gray—Macrophages in acute Allograft rejection. *Int. J. Mol. Sci.* **24**, 8257 (2023).
40. T. P. P. van den Bosch, K. Caliskan, M. D. Kraaij, A. A. Constantinescu, O. C. Manintveld, P. J. M. Leenen, J. H. von der Thüsen, M. C. Clahsen-van Groningen, C. C. Baan, A. T. Rowshani, $CD16^+$ monocytes and skewed macrophage polarization toward M2 type hallmark heart transplant acute cellular rejection. *Front. Immunol.* **8**, 346 (2017).
41. D. Toki, W. Zhang, K. L. M. Hor, D. Liuwantara, S. I. Alexander, Z. Yi, R. Sharma, J. R. Chapman, B. J. Nankivell, B. Murphy, P. J. O'Connell, The role of macrophages in the

development of human renal allograft fibrosis in the first year after transplantation. *Am. J. Transplant.* **14**, 2126–2136 (2014).
42. P. Italiani, D. Boraschi, From monocytes to M1/M2 macrophages: Phenotypical vs. functional differentiation. *Front. Immunol.* **5**, 514 (2014).
43. L.-X. Wang, S.-X. Zhang, H.-J. Wu, X.-L. Rong, J. Guo, M2b macrophage polarization and its roles in diseases. *J. Leukoc. Biol.* **106**, 345–358 (2019).
44. C. M. Schürch, S. S. Bhate, G. L. Barlow, D. J. Phillips, L. Noti, I. Zlobec, P. Chu, S. Black, J. Demeter, D. R. McIlwain, N. Samusik, Y. Goltsev, G. P. Nolan, Coordinated cellular neighborhoods orchestrate antitumoral immunity at the colorectal cancer invasive front. *Cell* **182**, 1341–1359.e19 (2020).
45. J. Windhager, V. R. T. Zanotelli, D. Schulz, L. Meyer, M. Daniel, B. Bodenmiller, N. Eling, An end-to-end workflow for multiplexed image processing and analysis. *Nat. Protoc.* **18**, 3565–3613 (2023).
46. E. B. Thorp, C. Stehlik, M. J. Ansari, T-cell exhaustion in allograft rejection and tolerance. *Curr. Opin. Organ Transplant.* **20**, 37–42 (2015).
47. C. Macedo, E. A. Orkis, I. Popescu, B. D. Elinoff, A. Zeevi, R. Shapiro, F. G. Lakkis, D. Metes, Contribution of naïve and memory T-cell populations to the human alloimmune response. *Am. J. Transplant.* **9**, 2057–2066 (2009).
48. M. Ningappa, C. Ashokkumar, B. W. Higgs, Q. Sun, R. Jaffe, G. Mazariegos, D. Li, D. E. Weeks, S. Subramaniam, R. Ferrell, H. Hakonarson, R. Sindhi, Enhanced b cell alloantigen presentation and its epigenetic dysregulation in liver transplant rejection. *Am. J. Transplant.* **16**, 497–508 (2016).
49. F. M. Bosisio, Y. Van Herck, J. Messiaen, M. M. Bolognesi, L. Marcelis, M. Van Haele, G. Cattoretti, A. Antoranz, F. De Smet, Next-generation pathology using multiplexed immunohistochemistry: mapping tissue architecture at single-cell level. *Front. Oncol.* **12**, 918900 (2022).
50. F. K. Baddoura, I. W. Nasr, B. Wrobel, Q. Li, N. H. Ruddle, F. G. Lakkis, Lymphoid neogenesis in murine cardiac allografts undergoing chronic rejection. *Am. J. Transplant.* **5**, 510–516 (2005).
51. N. H. Ruddle, Posttransplant tertiary lymphoid organs. *Transplantation* 10.1097/TP.0000000000004812, (2023).
52. A. I. Bery, H. M. Shepherd, W. Li, A. S. Krupnick, A. E. Gelman, D. Kreisel, Role of tertiary lymphoid organs in the regulation of immune responses in the periphery. *Cell. Mol. Life Sci.* **79**, 359 (2022).
53. E. Di Carlo, T. D'Antuono, S. Contento, M. Di Nicola, E. Ballone, C. Sorrentino, Quilty effect has the features of lymphoid neogenesis and shares CXCL13-CXCR5 pathway with recurrent acute cardiac rejections. *Am. J. Transplant.* **7**, 201–210 (2007).
54. D. Kerjaschki, H. M. Regele, I. Moosberger, K. Nagy-Bojarski, B. Watschinger, A. Soleiman, P. Birner, S. Krieger, A. Hovorka, G. Silberhumer, P. Laakkonen, T. Petrova, B. Langer, I. Raab, Lymphatic neoangiogenesis in human kidney transplants is associated with immunologically active lymphocytic infiltrates. *J. Am. Soc. Nephrol.* **15**, 603–612 (2004).
55. J. Kirveskari, T. Paavonen, P. Häyry, R. Renkonen, De novo induction of endothelial L-selectin ligands during kidney allograft rejection. *J. Am. Soc. Nephrol.* **11**, 2358–2365 (2000).
56. H. Nishimura, M. Nose, H. Hiai, N. Minato, T. Honjo, Development of lupus-like autoimmune diseases by disruption of the PD-1 gene encoding an ITIM motif-carrying immunoreceptor. *Immunity* **11**, 141–151 (1999).
57. D. L. Barber, E. J. Wherry, D. Masopust, B. Zhu, J. P. Allison, A. H. Sharpe, G. J. Freeman, R. Ahmed, Restoring function in exhausted CD8 T cells during chronic viral infection. *Nature* **439**, 682–687 (2006).
58. M. Eghtedari, C. McKenzie, J. Kench, 41. Banff global assessment and rejection activity index severity grading criteria for T-cell mediated rejection (TCMR) in liver transplantation are strongly correlated. *Pathology* **52**, S147 (2020).
59. M. Sorin, M. Rezanejad, E. Karimi, B. Fiset, L. Desharnais, L. J. M. Perus, S. Milette, M. W. Yu, S. M. Maritan, S. Doré, É. Pichette, W. Enlow, A. Gagné, Y. Wei, M. Orain, V. S. K. Manem, R. Rayes, P. M. Siegel, S. Camilleri-Broët, P. O. Fiset, P. Desmeules, J. D. Spicer, D. F. Quail, P. Joubert, L. A. Walsh, Single-cell spatial landscapes of the lung tumour immune microenvironment. *Nature* **614**, 548–554 (2023).
60. D. Wang, B. Eraslan, T. Wieland, B. Hallström, T. Hopf, D. P. Zolg, J. Zecha, A. Asplund, L. Li, C. Meng, M. Frejno, T. Schmidt, K. Schnatbaum, M. Wilhelm, F. Ponten, M. Uhlen, J. Gagneur, H. Hahne, B. Kuster, A deep proteome and transcriptome abundance atlas of 29 healthy human tissues. *Mol. Syst. Biol.* **15**, e8503 (2019).
61. S. A. MacParland, J. C. Liu, X. Z. Ma, B. T. Innes, A. M. Bartczak, B. K. Gage, J. Manuel, N. Khuu, J. Echeverri, I. Linares, R. Gupta, M. L. Cheng, L. Y. Liu, D. Camat, S. W. Chung, R. K. Seliga, Z. Shao, E. Lee, S. Ogawa, M. Ogawa, M. D. Wilson, J. E. Fish, M. Selzner, A. Ghanekar, D. Grant, P. Greig, G. Sapisochin, N. Selzner, N. Winegarden, O. Adeyi, G. Keller, G. D. Bader, I. D. McGilvray, Single cell RNA sequencing of human liver reveals distinct intrahepatic macrophage populations. *Nat. Commun.* **9**, 4383 (2018).
62. T. Hoch, D. Schulz, N. Eling, J. M. Gómez, M. P. Levesque, B. Bodenmiller, Multiplexed imaging mass cytometry of the chemokine milieus in melanoma characterizes features of the response to immunotherapy. *Sci. Immunol.* **7**, eabk1692 (2022).
63. A. Baranski, I. Milo, S. Greenbaum, J. P. Oliveria, D. Mrdjen, M. Angelo, L. Keren, MAUI (MBI Analysis User Interface)—An image processing pipeline for Multiplexed Mass Based Imaging. *PLOS Comput. Biol.* **17**, e1008887 (2021).
64. R. A. Amezquita, A. T. L. Lun, E. Becht, V. J. Carey, L. N. Carpp, L. Geistlinger, F. Marini, K. Rue-Albrecht, D. Risso, C. Soneson, L. Waldron, H. Pagès, M. L. Smith, W. Huber, M. Morgan, R. Gottardo, S. C. Hicks, Orchestrating single-cell analysis with Bioconductor. *Nat. Methods* **17**, 137–145 (2019).
65. N. Eling, N. Damond, T. Hoch, B. Bodenmiller, cytomapper: An R/Bioconductor package for visualization of highly multiplexed imaging data. *Bioinformatics* **36**, 5706–5708 (2021).
66. L. Van Der Maaten, G. Hinton, Visualizing Data using t-SNE. *J. Mach. Learn. Res.* **9**, 2579–2605 (2008).
67. L. Haghverdi, A. T. L. Lun, M. D. Morgan, J. C. Marioni, Batch effects in single-cell RNA-sequencing data are corrected by matching mutual nearest neighbors. *Nat. Biotechnol.* **36**, 421–427 (2018).
68. L. McInnes, J. Healy, N. Saul, L. Großberger, UMAP: Uniform manifold approximation and projection. *J. Open Source Softw.* **3**, 861 (2018).
69. G. Csardi, T. Nepusz, The igraph software package for complex network research. *InterJournal* **Complex Systems**, 1695 (2006), https://igraph.org.

Acknowledgments: We thank C. Blackwell for the contribution to the subanalysis reported in table S1. We would like to acknowledge the Bodenmiller Laboratory for hosting an IMC workshop and allowing us to participate and for helping us to customize our analysis pipeline. We thank the CHLA SC2 Core Facility for working with us to optimize our staining panel and for performing timely data acquisition. All main and extended data figures were created in BioRender, and we acknowledge the helpful tutorials and customer service (BioRender.com). **Funding:** B.R. was supported by the OneLegacy Fellowship Training Grant and the Broad Clinical Research Fellowship. B.G. was supported by grants from the National Institutes of Health (NIH) (R35GM137936 and P01HD106414). J.E. is supported by a K08 grant from the National Cancer Institute (K08CA245220); American Society of Transplant Surgeons Faculty Development Grant; Society for the Study of Liver Diseases, Clinical, Translational, and Outcomes Research Award; and Liver Scholar Award from Gilead Research Foundation. We also received a substantial investment in research from the Abdominal Organ Transplant Program at Children's Hospital–Los Angeles to develop our IMC panel and analysis pipeline. **Author contributions:** Conceptualization: A.B., B.R., S.B., O.A., R.K., L.S., and J.E. Methodology: A.B., B.R., S.B., J.K., and S.C. Investigation: A.B., B.R., S.B., C.W., S.C., K.S., B.G., and J.E. Visualization: A.B., B.R., S.B., R.K., S.C., O.A., K.S., B.G., and J.E. Supervision: J.E. Writing—original draft: A.B., B.R., S.B., and J.E. Writing—review and editing: All contributing authors. **Competing interests:** R.K. receives funds from Epigen Biosciences (R44) and serves in the advisory board of Ipsen Biopharmaceuticals and Mirum Pharmaceuticals. All other authors declare that they have no competing interests. **Data and materials availability:** All data needed to evaluate the conclusions in the paper are present in the paper and/or the Supplementary Materials. Data to reproduce the findings in this study, including high-dimensional TIFF images, are available on our GitHub and accessible via Zenodo (DOI: 10.5281/zenodo.10552911). The external dataset used as part of the nCounter transcriptomic analysis is available in the Supplementary Materials (multimedia component 3) from T.Y. Lim *et al.* (https://doi.org/10.1016/j.jhep.2022.08.035) (*31*). All scripts to analyze data and reproduce the results showed in the present study are available on our GitHub (https://github.com/julietusc/IMC_liver_rejection_adults) and accessible via Zenodo (DOI: 10.5281/zenodo.10552911).

Submitted 10 November 2023
Accepted 12 March 2024
Published 12 April 2024
10.1126/sciadv.adm8841